

Formulations of Hydrodynamic Force in the Transition Stage of the Water Entry of Linear Wedges with Constant and Varying Speeds

Xueliang Wen^a, Peiqing Liu^a, Alessandro Del Buono^b, Qiulin Qu^a, Alessandro Iafrati^b

^a*School of Aeronautic Science and Engineering, Beihang University, Beijing, 100191, China*

^b*CNR-INM, Via di Vallerano 139, 00128 Rome, Italy*

Abstract

There is an increasing need to develop a two-dimensional (2D) water entry model including the slamming and transition stages for the 2.5-dimensional (2.5D) method being used on the take-off and water landing of seaplanes, and for the strip theory or 2D+t theory being used on the hull slamming. Motivated by that, this paper numerically studies the transition stage of the water entry of a linear wedge with constant and varying speeds, with assumptions that the fluid is incompressible, inviscid and with negligible effects of gravity and surface tension, and the flow is irrotational. For the constant speed impact, the similitude of the declining forces of different deadrise angles in the transition stage are found by scaling the difference between the maximum values in the slamming stage and the results of steady supercavitating flow. The formulation of the hydrodynamic force is conducted based on the similitude of the declining forces in the transition stage together with the linear increasing results in the slamming stage. For the varying speed impact, the hydrodynamic force caused by the acceleration effect in the transition stage is formulated by an added mass coefficient with an averaged increase of 27.13% compared with that of slamming stage. Finally, a general expression of the hydrodynamic forces in both the

*Qiulin Qu

Email addresses: wenxueliang@buaa.edu.cn (Xueliang Wen), lpq@buaa.edu.cn (Peiqing Liu), alessandro.delbuono@inm.cnr.it (Alessandro Del Buono), qq1@buaa.edu.cn (Qiulin Qu), alessandro.iafrati@cnr.it (Alessandro Iafrati)

slamming and transition stages is thus proposed and has good predictions in the ranges of deadrise angles from 5° to 70° for both the constant and varying speed impacts.

Keywords: water entry, wedge, hydrodynamic force, transition stage

Nomenclature

| | | |
|------------------------------------|---|--|
| \mathbf{a} | = | Accelerations of body |
| a_w | = | Acceleration of body in vertical direction |
| A | = | Dimensionless variable of the theory of steady supercavitating flow |
| A_2, B_2 | = | Dimensionless variables of approximate solution |
| $A_{2\text{Mei}}, B_{2\text{Mei}}$ | = | Dimensionless variable of Mei et al.'s model |
| c | = | Effective wetted length |
| C_a | = | Added mass coefficient |
| C_{a0} | = | $A_2(k_2 \tan \beta)^2$ Added mass coefficient in the slamming stage |
| C_{const} | = | Dimensionless coefficient of constant speed impact |
| C_{Korobkin} | = | C_{const} of Korobkin's model |
| C_p | = | Pressure coefficient |
| C_{p0} | = | Pressure coefficient of constant speed impact |
| c_q | = | Volume fraction of q^{th} fluid |
| C_s | = | Slamming coefficient |
| C_{s0} | = | Slamming coefficient of constant speed impact |
| C_{s0}^* | = | $(C_{s0} - C_{s\infty}) / (C_{s\text{max}} - C_{s\infty})$ |
| $C_{s\text{max}}$ | = | Maximum Slamming coefficient |
| $C_{s\infty}$ | = | Slamming coefficient of steady supercavitating flow |
| $f_{3\text{D}}$ | = | Force coefficient of 3D effect |
| F | = | Force acting on bodies in vertical direction |
| \mathbf{F} | = | Total hydrodynamic forces acting on the body surface |
| F_0 | = | Force acting on bodies of constant speed impact |
| Fr | = | U_0 / \sqrt{gl} Froude number of the freefall motion case |
| g | = | Gravitational acceleration |

| | | |
|--------------|---|--|
| \mathbf{g} | = | Body forces in Euler equations |
| G | = | Core function of the second Green identity |
| h | = | Penetration depth |
| h_0 | = | $l \tan \beta$ Height of wedge |
| h_2 | = | Penetration depth corresponding to $C_{s\max}$ |
| h^* | = | $(h - h_2)/h_2 \cot^\lambda \beta$ |
| k | = | Parameter of curved FBC |
| k_1 | = | h_2/h_0 Dimensionless penetration depth of the maximum C_{s0} |
| k_2 | = | $\frac{\partial C_{s0}}{\partial (h/h_0)}$ Dimensionless derivative of C_{s0} with respect to h |
| l | = | Half width of a finite body |
| L | = | Thickness of a 3D wedge |
| m | = | Mass of the wedge |
| m_0 | = | Added mass of wedge in half model |
| \mathbf{n} | = | Unit vector of normal to the wall surface |
| n_y | = | Projection in vertical direction y of \mathbf{n} |
| N | = | Number of nodes to calculate parameter n |
| p | = | Pressure |
| p_0 | = | Pressure of constant speed impact |
| p_a | = | Atmosphere pressure |
| \bar{P} | = | Vertices of the lower side in jet region |
| \bar{P} | = | Vertices of the upper side in jet region |
| r | = | Ratio between the normal distance between the two side of the jet in proximity of the spray root and the minimum panel size |
| t | = | Time |
| \mathbf{u} | = | $\nabla \phi$ Velocities of fluid |
| u_n, u_s | = | Normal and tangential projections of fluid velocity on the body surface |
| U_0 | = | Initial speed of wedge |
| U_w | = | Instantaneous speed of wedge |
| v | = | Fluid velocity of the theory of steady supercavitating flow |
| v_0 | = | Incoming velocity of water of steady supercavitating flow |

| | | |
|----------------------|---|--|
| \mathbf{V}_q | = | Velocities of the q^{th} fluid |
| v_n | = | Vertical velocity on the free surface |
| \mathbf{V} | = | Velocities of fluid |
| w_n, w_s | = | Normal and tangential projections of body speeds on the body surface |
| \mathbf{W} | = | Body speeds |
| \mathbf{x} | = | Position of particles lying on the free surface |
| $x, y,$ | = | Cartesian coordinates |
| z | = | $x + iy$ Complex coordinates |
| $\alpha, \chi, \mu,$ | = | Coefficients of the velocity potential expression in the jet region |
| β | = | Deadrise angle of wedge bodies |
| β_L | = | Deadrise angle of linear FBC |
| Δp | = | Difference of pressure between the constant and varying speed impacts |
| ΔF | = | Difference of force between the constant and varying speed impacts |
| η | = | $\frac{1}{N} \sum_{i=1}^N \sigma_i^2$ Mean σ of all the nodes in $h^* \in [0, 7]$ |
| γ | = | Correction factor of wetted length |
| γ_{Mei} | = | Correction factor of wetted length for Mei et al.'s model |
| κ | = | Growth factor of BEM-FEM panels |
| λ | = | Auxiliary variable to model the C_{s0} in the transition stage |
| ω | = | Parameter complex plane |
| ϕ | = | Velocity potential |
| ϕ_0 | = | Velocity potential at C and C' in the theory of steady supercavitating flow |
| Φ | = | Dimensionless velocity potential of similarity solution |
| ρ | = | Density of water |
| σ | = | Standard deviation of C_{s0}^* between different deadrise angles |
| τ | = | Parameter complex plane |
| θ | = | Argument of the velocity of fluid |
| <i>Superscript</i> | | |
| J | = | Panel in the jet region |
| * | = | Variables at the centroid of fluid control volume |
| <i>Subscript</i> | | |

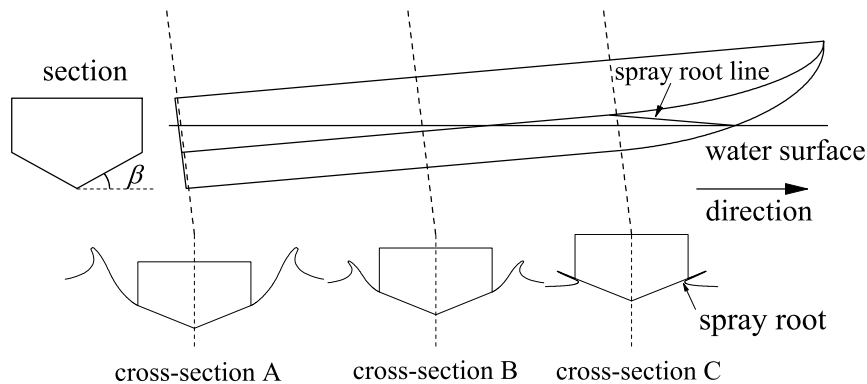


Fig. 1: The free surfaces of different cross-sections of a hull during the high speed planning.

- q = Phase of fluid
- i = Index of vertices in the jet region or index of node

1. Introduction

The take-off and water-landing of seaplanes had been studied since 1920s and the procedures to assess the structural crashworthiness of airframe is mainly based on a 2.5-dimensional (2.5D) method [1, 2, 3], which is similar to the formulations of slamming forces of the strip theory for the hull slamming. Every individual cross-section normal to the longitudinal direction of hull independently experiences a single process of water entry (see Fig.1), where the 2D water entry model is formulated by the added mass method [4, 1, 2] or the Wagner theory [5, 3]. The traditional procedures had been identified to be less accurate as the numerical methods have fast developed in recent decades, and make it possible to conduct numerical simulations of water-landing of seaplanes [6] and transport airplanes [7, 8]. Although a whole-time history of water entry of aircraft can be reproduced, massive computational resources are required and several days of calculations are taken. This could not be treated as a practical method for the engineers to complete the initial designs of seaplanes or high-speed planning hulls [9, 10]. The alternative method is to improve the 2D

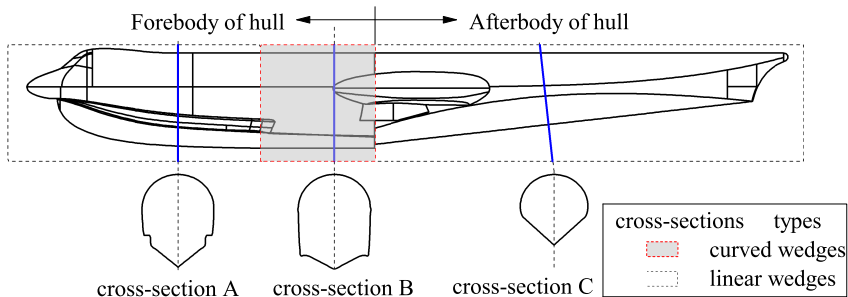


Fig. 2: The cross-sections (normal to the keels) of the hull of seaplanes.

model of the 2.5D methods because the errors of early 2.5D methods are mainly resulted from the transverse pressure distribution, especially for that with chine immersion. For the cross-section C Fig. 1 without chine immersion, they used the Wagner theory; For the cross-sections A and B in Fig. 1 with chine immersion, they adopted the pressure distribution of a steady supercavitating flow [11, 12] to formulate the transverse flow. However, the pressure distribution of Wagner theory is quite different from that of steady supercavitating flow. How the pressure distribution continuously changes from that of Wager theory to that of steady supercavitating flow is missing in the early 2.5D methods.

From the perspective of a 2D transverse flow in a constant speed, the cross-section without chine immersion is corresponding to a slamming stage in which the hydrodynamic force increases linearly with the increasing wetted length, and the cross-section with chine immersion is corresponding to a transition stage in which the body experiences a fast drop of hydrodynamic force when the spray root leaves the chine. The pressure distribution and the hydrodynamic force gradually decline and finally approach those of steady supercavitating flow, as the experimental results of Zhao et al. [13] indicated. The poor accuracy of original 2.5D methods is due to the weakness of their 2D model for the transverse flow and lack of involvement of the hydrodynamic forces acting on afterbody of hull (see Fig. 2). Since there is no effective theoretical method to formulate the transition stage, Sun and Faltinsen [14, 15] directly adopted a boundary element method (BEM) as the 2D water entry model to develop another similar

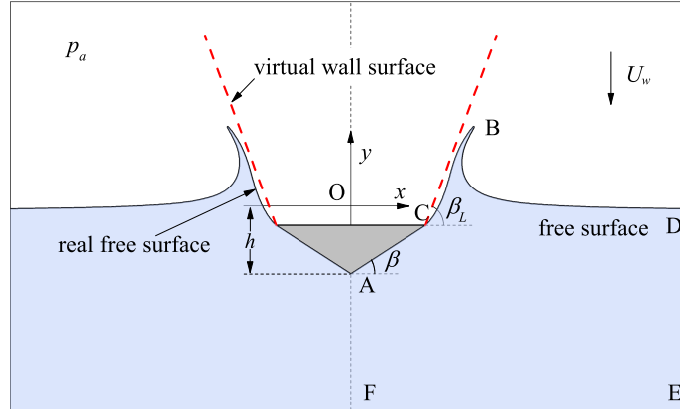


Fig. 3: The description of the water entry of a 2D wedge with a speed of U_w , h being the penetration depth.

method called 2D+t theory for the high speed hulls. Their BEM [16, 13] can address both the slamming and transition stages with increasing accuracy of predictions, but at the same time greatly increases the computational cost, which undermines the efficiency of the 2D+t theory. Therefore, there is an increasing need to improve the efficiency of the 2.5D methods and the 2D+t theory by proposing an analytical solution as accurate as the numerical methods to predict the hydrodynamic forces in both slamming and transition stages. For the slamming stage, many researchers had contributed to the formulations of hydrodynamic force by added mass methods [4, 5, 17], asymptotic theories [18, 19, 20] and approximate solution [21]. Among them, the approximate solution of Wen et al.[21] provided the most accurate model for the constant and varying speed cases by a similarity solution of Dobrovoll'skaya[22]. For the transition stage, due to the different hydrodynamic characteristics, the formulation of hydrodynamic force is more difficult and is yet to be fully addressed. In this paper, by following the formulation work of our previous research [21], the transition stage of the water entry of linear wedges with constant and varying speeds, as shown in Fig. 3, is formulated to complete the 2D water entry model.

There are three different formulations of the hydrodynamic forces in the

transition stage in literature. The first one was proposed by Logvinovich[18] based on the boundary condition at the separation (point C in Fig. 3). The pressure at C is required to be same with the atmospheric pressure, which is denoted as zero pressure condition. Logvinovich derived an ordinary differential equation (ODE) to obtain a virtual wetted length but integrated the pressure to obtain the hydrodynamic force on the real wetted surface AC. Tassin et al. [23] improved the Logvinovich’s model by introducing the correction of $1+\tan^2 \beta$ (β being the deadrise angle) to the pressure expression on the wall surface and re-derived the ODE of virtual wetted length. The predictions are in better agreement with BEM results of Iafrati and Battistin [24] than the original one. The second way is called fictitious body continuation (FBC) and was also developed by Tassin et al. [23] based on a modified Logvinovich’s model (MLM) of Korobkin [20] who addressed the formulation of the slamming stage. The FBC is a virtual wall surface extended from the separation C with an angle of β_L with respect to the horizontal line (see Fig. 3). The wetted length is solved from the combination of the real wall surface AC and FBC, while the hydrodynamic force is only integrated on AC as it does in the Logvinovich’s model of the zero pressure condition. Tassin et al. [23] had to compare with the numerical results to identify the parameter β_L . Although the agreement with the numerical results is better than the Logvinovich’s model with correction $1+\tan^2 \beta$, there is still some discrepancy and the FBC needs more improvement. Wen et al. [25] proposed the curved FBC to improve the accuracy of linear FBC of Tassin et al. [23] based on a modified Wagner’s model (MWM). They introduced another parameter k and provided explicit equations to determine β_L and k . Their predictions were in better agreement with the numerical results than the linear FBC of Tassin et al. [23]. Since these methods are all based on the Wagner theory [5], their predictions will become less accurate when the deadrise angle is larger than 30° . The last and the most sophisticated formulation was conducted by Semenov and Wu [26] by extending their integral hodograph method (IHM) [27, 28] from the slamming stage to transition stage. Their results show a larger declining force than the BEM simulations of Iafrati and Battistin [24] because

they imposed a self-similar solution onto a non-self-similar flow in the transition stage. In general, the fully analytical solutions as accurate as the numerical results and with a range of deadrise angle $[15^\circ, 45^\circ]$ for the applications of take-off and water landing of seaplanes are currently unavailable. In contrast to formulate the hydrodynamic force by the asymptotic analysis and self-similar solution, a semi-analytical solution for both the slamming and transition stages can be probably built by summarizing the numerical results and exploring the possible patterns of the hydrodynamic forces.

The failures of the abovementioned theoretical methods to formulate the hydrodynamic forces in the transition stage is caused by inaccurate modelling of free surface, which is the main difference between the numerical methods and the theoretical methods. There are two broad categories of the numerical methods: BEM and computational fluid dynamics (CFD). The free surface problems of water entry for the BEM include the modelling of jet and the new free surface AC. Zhao et al. [13] provided the first fully nonlinear BEM results, using a model of jet-cut to avoid the high-speed thin jet, and the lowest-order expansion of the Kutta condition (the flow leaves the body tangentially at the separation point C) to simplify the new free surface AC. Iafrati and Battistin [24] proposed a different approach to switch boundary conditions (BCs) of the panels from a wall panel to a free surface panel when the center of panel leaves the separation point C. Instead of using the jet cutting strategy as Zhao and Faltinsen [16] and their previous method [29] did, they combined the use of a BEM solver in the bulk of fluid and a simplified finite element method (FEM) in the thin jet developing along the body contour. The hybrid method was denoted as a hybrid BEM-FEM (HBF) approach and can provide a detailed description of the flow and free surface dynamics, together with an improved prediction of the separation, while keeping the computational effort still reasonable. The HBF method was recently extended by Del Buono et al. [30] to deal with the water entry with varying speed and the water exit problems. Considering the good application of the BCs switching, Wang and Faltinsen [31] also develop their BEM of jet cutting replacing the lowest-order expansion of the Kutta condition with the

BCs switching for the water entry problems. In contrast to the BCs switching and FEM solver, Bao et al. [32] used the least orders of equations to update the normal velocity of the free surface AC and a shallow water assumption for the jet region in the transition stage. The abovementioned BEM methods have different strategies for the jet region and new free surface AC, but are basically consistent with each other. They can reduce the computational cost and provide the velocity potential distribution on the wedge surface, which is important for the varying speed impact. Different from the complexity of the free surface modelling of BEM, the CFD methods are more flexible to deal with the modelling of free surface. The most widely used method for the free surface problems, volume of fraction (VOF), was first proposed by Hirt and Nichols [33] based on the framework of finite volume method (FVM). A modified high-resolution interface capturing scheme (Modified HRIC) was developed by Muzaferija et al. [34] to solve volume fraction equations and has good applications to the water entry problems [8, 35, 36]. Compared with the BEM approaches, the CFD methods provide more information about the distributions of pressure and velocities in the whole region which intuitively picture the rapid changes of flow field in the transition stage of the constant speed impact. The FVM with VOF has been the most successful method to deal with the water entry problems and will be adopted in this paper to produce the numerical results of constant speed impact. In order to study the distribution of velocity potential on the wall surface for the varying speed impact, the HBF of Iafrati and Battistin [24] will also be used to provide the required data.

In this paper, the slamming and transition stages of water entry of linear wedges with constant and varying speeds are numerically studied by the FVM with VOF [36] and the HBF of Iafrati and Battistin [24]. To propose a semi-analytical solution of a combination of numerical results and theoretical results to address the high speed impact problems, the fluid is considered to be incompressible, non-viscous, weightless and with negligible surface tension effects and the flow is to be irrotational. The hydrodynamic forces in the slamming and transition stages during the water entry of a wedge with constant and varying

speeds will be formulated. The arrangements of this paper are as follows. The computational approaches of FVM with VOF and HBF are detailed in Sec.2 and the validations of the two methods are given in Sec.3. For the constant speed impact, the formulation of forces in both slamming and transition stages of the water entry of linear wedges with the deadrise angles varying from 5° to 70° is proposed based on the CFD results in Sec.4. For the varying speed impact, the acceleration effect is addressed based on the HBF results in Sec.5. The general formulations of hydrodynamic force of both the slamming and transition stages will be provided and can address the constant speed impact and the acceleration effect.

2. Computational Approaches

A CFD method of FVM with VOF technique is adopted to provide the detailed results of flow field of water entry in a constant speed and the HBF [24, 37] is used to calculate the velocity potential (the CFD method can't provide the velocity potential) and the pressure distributions on the wedge surface during the water entry in a varying speed.

2.1. CFD method

2.1.1. Flow solver

The unsteady incompressible Euler equations ignoring the surface tension force are solved using ANSYS FLUENT as follows

$$\frac{\partial \mathbf{V}}{\partial t} + \mathbf{V} \cdot \nabla \mathbf{V} = -\frac{1}{\rho} \nabla p - \mathbf{g}, \quad (1)$$

where \mathbf{V} is the velocity of fluid, ρ is the density, p is the pressure and $\mathbf{g} = (0, -g)$ representing the gravity of fluid (the gravity of fluid can be neglected for the high speed impact). The semi-implicit method for pressure linked equation consistent algorithm (SIMPLEC) is used to deal with the pressure-velocity coupling. The unsteady terms are discretized by first order implicit scheme, the convection terms are discretized by second order upwind scheme, and the pressure term is discretized by body force weighted scheme.

2.1.2. VOF method

The VOF method was firstly proposed by Hirt and Nichols [33], which can capture the free interfaces between two or more immiscible fluids by introducing a variable, called volume fraction, for each phase. If the volume fraction of the q^{th} fluid in a certain cell is denoted as c_q , $c_q = 0$ represents the cell is empty of the q^{th} fluid; $c_q = 1$ represents the cell is full of the q^{th} fluid; and $0 < c_q < 1$ represents the cell contains the interface between the q^{th} fluid and other fluids. The sum of the volume fractions of all phases must be 1 in each cell. The volume fraction equation of the q^{th} fluid is written as follows:

$$\frac{\partial}{\partial t}(c_q \rho_q) + \nabla \cdot (c_q \rho_q \mathbf{V}_q) = 0, \quad (2)$$

where \mathbf{V}_q is the velocity of q fluid. The first term in the left hand is discretized by one order implicit scheme, and the second term is discretized by modified high resolution interface capturing (Modified HRIC) scheme [34].

2.1.3. GMM method and VOF boundary conditions

In this paper, the global moving mesh method (GMM) [38] is used to deal with the motion of wedge. The whole computational domain (including the cells and boundaries) moves together with the wedge like a rigid body. The volume fraction boundary conditions can ensure that the free water surface keeps a given level when the computational domain moves. This condition is set according to the cell coordinates of the boundaries in the earth fixed coordinate system, i.e., the volume fraction of water $c_q = 0.5$ for the cell located on the interface between air and water; $c_q = 0$ for the cells located above the interface; $c_q = 1$ for the cells located below the interface.

2.2. HBF approach

In this section, the fully nonlinear potential flow model based the hybrid BEM-FEM approach is presented. The method is mainly based on the studies of Refs. [24, 37], where full details are provided.

2.2.1. Governing Equations

The water entry problem of rigid bodies is faced under the hypotheses of an inviscid and incompressible fluid. The flow is assumed irrotational and the problem is formulated in terms of the velocity potential ϕ . Surface tension effects are neglected. The flow is therefore governed by the following initial-boundary value problem:

$$\nabla^2 \phi = 0 \quad \text{in water domain } \Omega, \quad (3)$$

$$\frac{\partial \phi}{\partial n} = \mathbf{W} \cdot \mathbf{n} = -U_w n_y \quad \text{on wall surface } S_B, \quad (4)$$

$$\frac{D\phi}{Dt} = \frac{|\nabla\phi|^2}{2} - gy, \quad \frac{D\mathbf{x}}{Dt} = \nabla\phi, \quad \text{on free surface } S_S, \quad (5)$$

where \mathbf{n} is the unit vector of normal to the wall surface, n_y is the projection of \mathbf{n} in the vertical direction y , \mathbf{W} is the entering speed of the body, and \mathbf{x} is the position of the particle lying on the free surface. At each time step, the solution of the boundary-value problem for the velocity potential is solved in the form of the boundary integral representation provided by the second Green's identity

$$\frac{1}{2}\phi(P) = \int_{S_B \cup S_S} [\phi_n(Q) G(P, Q) - \phi(Q) G_n(P, Q)] dS(Q), \quad P \in S_B \cup S_S \quad (6)$$

where $G(P, Q) = \frac{1}{2\pi} \log(|P - Q|)$. According to Eqs. (4)-(5), the velocity potential is known on the free surface while its normal derivative is assigned on the body contour, which belongs to a boundary integral equation of mixed first and second kind. Once Eq. (6) is solved, the velocity potential and its normal derivative are known on the body contour and the free surface. The solution of the boundary integral equation Eq. (6), providing the normal derivative of the velocity potential on the free surface, allows the determination of the velocity field on the free surface, which is integrated in time through a two-step Runge-Kutta scheme to update the position of particle of the free surface.

2.2.2. Pressure distribution

The pressure distribution along the body contour is obtained through the Bernoulli's equation:

$$p - p_a = -\rho \left(\dot{\phi} + \frac{|\nabla\phi|^2}{2} + gy \right), \quad (7)$$

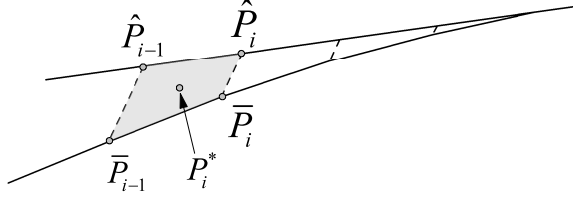


Fig. 4: The description of the jet model of the simplified FEM solver.

and the total hydrodynamic load is obtained by integration of the pressure field along the wetted part of the body

$$\mathbf{F} = - \int_{S_B} (p - p_a) \mathbf{n} dS. \quad (8)$$

$\dot{\phi}$ has to be provided before the pressure distribution on the wall surface is given. The calculation of $\dot{\phi}$ is similar to ϕ . On the free surface, the $\dot{\phi}$ is known as $\dot{\phi} = -\frac{|\nabla\phi|^2}{2} - gy$ according to Eq. (5). On the wall surface, the normal derivative of $\dot{\phi}$ is known and calculated as

$$\frac{\partial \dot{\phi}}{\partial n} = \mathbf{a} \cdot \mathbf{n} - w_s \frac{\partial u_n}{\partial s} - w_n \frac{\partial u_s}{\partial s} + k_s \mathbf{W} \cdot \mathbf{u}, \quad (9)$$

where \mathbf{a} is the body acceleration, w_s and w_n are the tangential and normal projections of \mathbf{W} on the wall surface, u_s and u_n are the tangential and normal projections of $\mathbf{u} = \nabla\phi$ on the wall surface and k_s denotes the curvature of the wall surface. The normal derivative of $\dot{\phi}$ on free surface and the $\dot{\phi}$ on the wedge surface can be solved by a similar boundary integral equation of Eq. (6). It is worth noting that the gravitational acceleration g is only used for the validations of freefall cases in Figs. 10 and 25, and is never included in other cases.

2.2.3. Jet model

In the simplified FEM solver used for the description of the thin jet, a part of the jet region is divided in control volumes in which the vertices corresponding to the panel centroids (\bar{P}_{i-1} , \bar{P}_i , \hat{P}_{i-1} , \hat{P}_i), as shown in Fig. 4. In each control volume, the velocity potential is written in the form of a harmonic polynomial expansion, up to second order. Details about the approach in the slamming

stage can be found in Battistin and Iafrati [24] and Del Buono et al. [30]. For the transition stage, the harmonic polynomial expansion, ϕ_i^J is reduced to first orders and reads

$$\phi_i^J(x, y) = \alpha_i + \chi_i(x - x_i^*) + \mu_i(y - y_i^*). \quad (10)$$

The corresponding normal derivative is

$$\phi_{n,i}^J(x, y) = \chi_i n_{x,i} + \mu_i n_{y,i} \quad (11)$$

where (x_i^*, y_j^*) is the centroid of the fluid control volume P_i^* , $n_{x,i}$ and $n_{y,i}$ are the unit vector of the i^{th} panel which are directed along the x -axis and y -axis, α_i , χ_i and μ_i are new unknown variables and can be determined by enforcing the free surface condition

$$\phi_i^J(\bar{P}_{i-1}) = \phi(\bar{P}_{i-1}), \quad \phi_i^J(\bar{P}_i) = \phi(\bar{P}_i), \quad (12)$$

and by enforcing the continuity of the ϕ_n at adjacent elements

$$\phi_{n,i}^J(\bar{P}_{i-1}) = \phi_{n,i-1}^J(\bar{P}_i). \quad (13)$$

3. Validations of numerical methods

3.1. Grid independence

Figure 5 shows the grid independence validation of the CFD simulations for the water entry of a wedge with $\beta = 30^\circ$ in a constant speed, where the slamming coefficient C_s and pressure coefficient C_p are defined as follows

$$C_s = \frac{F}{\frac{1}{2}\rho U_w^2 l}, \quad (14)$$

$$C_p = \frac{p - p_a}{\frac{1}{2}\rho U_w^2}, \quad (15)$$

where U_w is the entering speed of the body. Three grids of cell numbers of 50,000, 100,000 and 200,000 are adopted to simulate the impact flow with adaptive time steps. The courant number is set to be 0.95 during the adaptive time steps. The C_s of the whole time-history between the three grids match well. The C_p

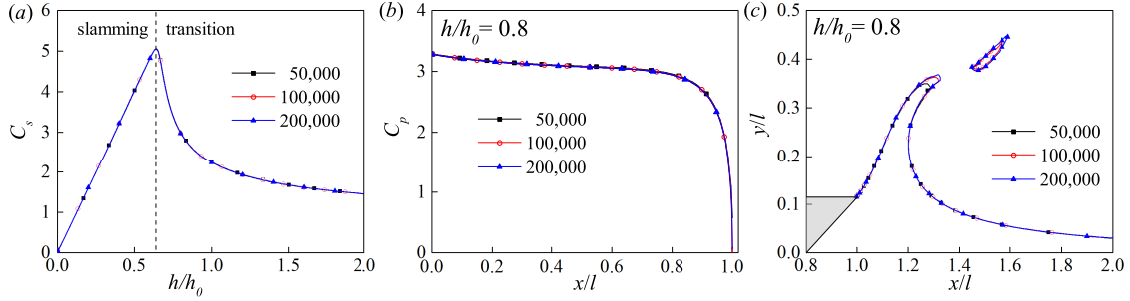


Fig. 5: Grid independence validation of the CFD simulations for the water entry of a wedge with $\beta = 30^\circ$ in a constant speed: (a) Slamming coefficient C_s ; (b) C_p distribution of $h/h_0 = 0.8$; Free surface of $h/h_0 = 0.8$.

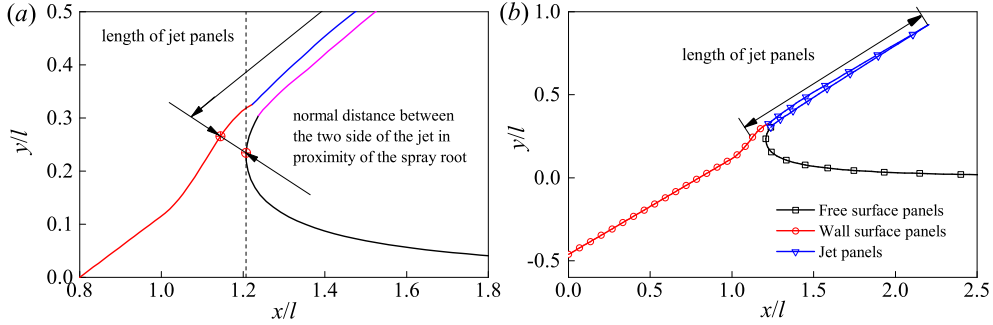


Fig. 6: Description of the BEM panels and FEM panels in the BEM.

distribution and free surface of $h/h_0 = 0.8$ ($h_0 = l \tan \beta$) are also consistent between the three grids except for some discrepancies at the tip of jet. The grid independence of CFD method is successfully validated. Therefore, the CFD grid with cell number of 100,000 is adopted for further simulations by balancing both the accuracy of spatial resolution and the computational cost.

Figure 6 shows the description of the HBF model in which the fluid boundary is divided into three parts: (1) free surface panels; (2) wall surface panels and (3) jet panels. The free surface and wall surface panels are solved by BEM solver while the jet panels are solved by the FEM solver. The panel distribution is determined by three parameters in Tab. 2: growth factors κ of BEM panels and FEM panels, as well as the ratio r between the normal distance between

| Grids | κ of BEM panels | κ of FEM panels | r |
|--------|------------------------|------------------------|-----|
| Coarse | 1.04 | 1.05 | 1.5 |
| Normal | 1.03 | 1.04 | 2.0 |
| Fine | 1.02 | 1.03 | 4.0 |

Tab. 2: The grid details of BEM panels: κ being the growth factor; r being the ratio between the normal distance between the two side of the jet in proximity of the spray root and the minimum panel size.

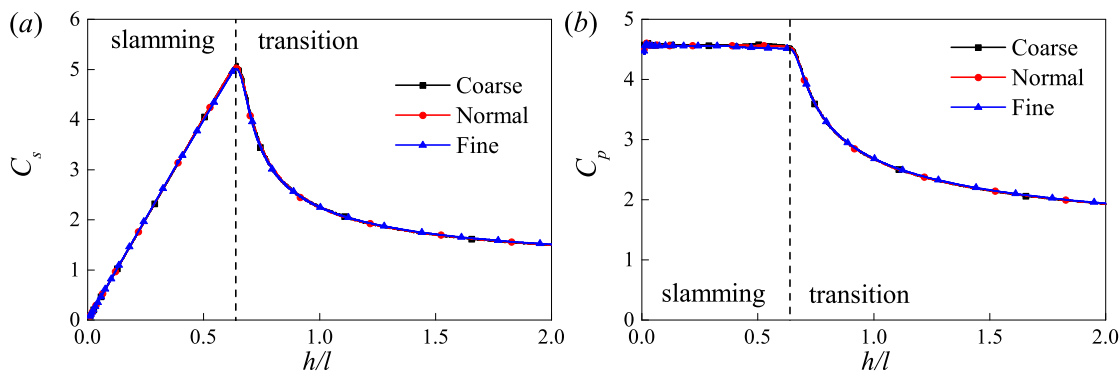


Fig. 7: The grid independence of the HBF simulations for the water entry of a wedge with $\beta = 30^\circ$ in a constant speed: (a) the slamming coefficient C_s ; (b) the pressure coefficient C_p at the tip of wedge.

the two side of the jet in proximity of the spray root and the minimum panel size. The C_s and C_p at the tip of wedge of the three distributions of HBF for the constant speed case in Fig. 7 match well with each other. Here, a normal grid is adopted for most of the HBF calculations in present study.

3.2. Comparisons between different methods

For the slamming stage of constant speed impact in which the self-similar flow is satisfied, the present CFD and HBF methods are compared with the similarity solution of Dobrovol'skaya[22, 36]. For the varying speed impact of both the slamming and transition stages, the present CFD and HBF methods are compared with the predictions of Bao et al.'s BEM [32] for the freefall motion

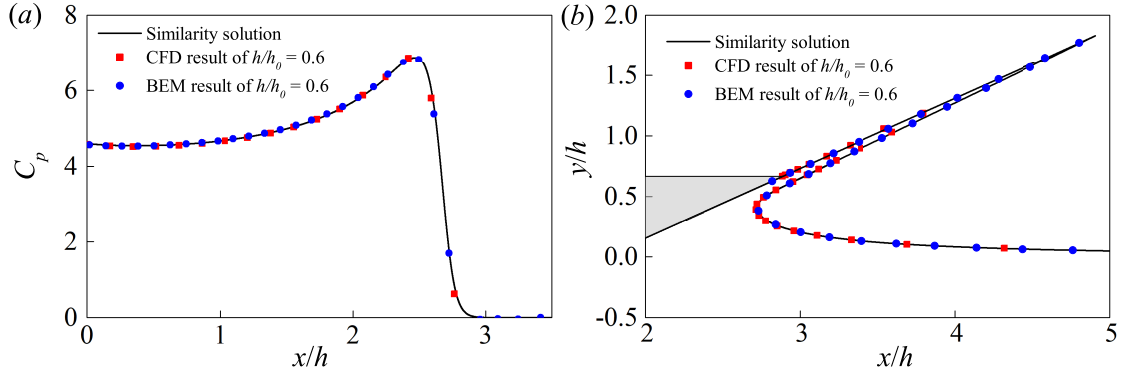


Fig. 8: The comparisons of the pressure coefficient C_p on the wedge surface and the free surface profiles of $h/h_0 = 0.6$ between the predictions of CFD, HBF and similarity solution [36] during the water entry of a wedge with $\beta = 30^\circ$ in a constant speed.

case. In this case, the impact speed is small and the gravity effect will become significant in the transition stage. In the simulations of Bao et al.'s case [32], the gravity of fluid is included. For the other cases, the gravity of fluid is excluded.

For the slamming stage with $h/h_0 = 0.6$ in the case of the water entry of a wedge with $\beta = 30^\circ$ in a constant speed, Fig. 8 shows the comparisons of the pressure coefficient C_p on the wedge surface and the free surface profiles between the predictions of CFD, HBF and similarity solution [36]. The spray root of the jet remains under the knuckle of the wedge, which means the self-similar flow is still satisfied and thereby the similarity solution can be used for a validation. The good agreement between the present methods and the similarity solution is excellent.

For the transition stage, Fig. 9 shows the comparisons of the force (a), pressure distribution (b) and free surface (c) between the present CFD and HBF for the water entry of a wedge with $\beta = 30^\circ$ in a constant speed. The CFD results are all consistent with those of HBF, except for the jet tip of free surface. Since the jet tip is of little relevance with the pressure and force acting on the wedge surface, the mutual validations between the present CFD and HBF are properly conducted. Fig. 10 shows the comparisons of the acceleration (a), pressure

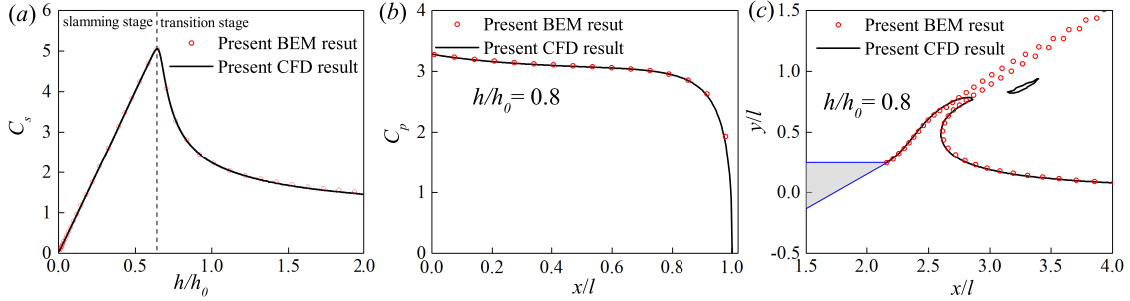


Fig. 9: Comparisons of the force (a), pressure distribution (b) and free surface (c) between the present CFD and HBF for the water entry of a wedge with $\beta = 30^\circ$ in a constant speed.

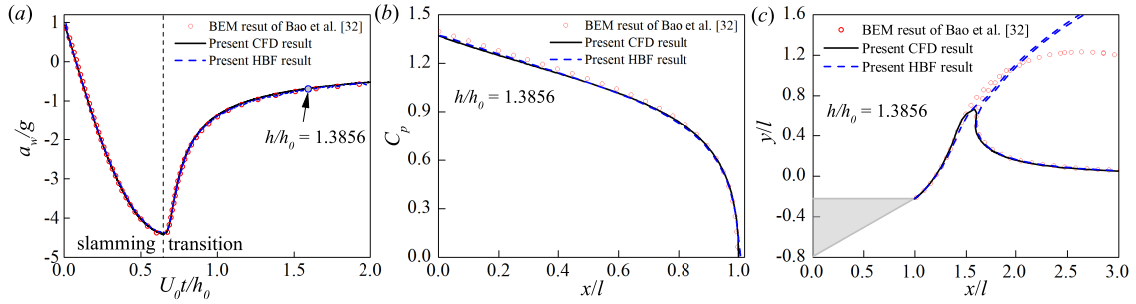


Fig. 10: Comparisons of the acceleration (a), pressure distribution (b) and free surface (c) between the CFD, HBF and BEM of Bao et al. [32] for the water entry of wedges of $\beta = 30^\circ$ in a freefall motion.

distribution (b) and free surface (c) between the CFD method, HBF and BEM of Bao et al. [32] for the water entry of wedges of $\beta = 30^\circ$ in a freefall motion. The CFD and HBF results are in good agreement with those of the BEM of Bao et al. [32], while there are still minor discrepancies of the jet tip of free surface and the pressure distribution near the apex of wedge. These differences are acceptable for the validations of CFD and HBF methods.

It can be concluded that the CFD method and HBF method are consistent with each other and can deal with the slamming and transition stages of the constant and varying speed impacts. In this paper, the CFD method is mainly used to produce the numerical results of constant speed impact, while the HBF method is to used produce those of varying speed impact.

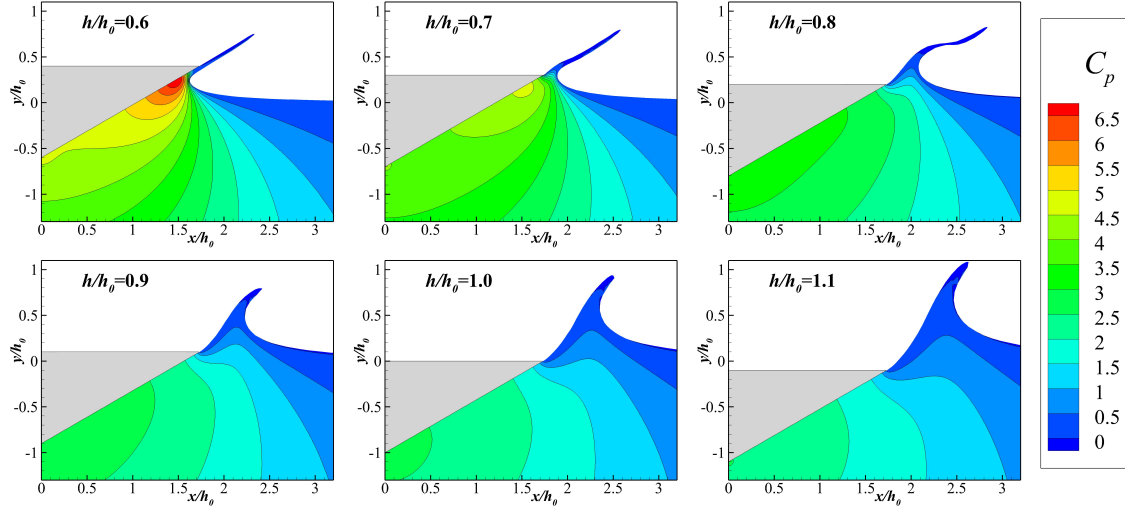


Fig. 11: The pressure distributions and free surface of different penetration depths in the transition stage during the water entry of a wedge with $\beta = 30^\circ$ in a constant speed [25].

4. Constant speed impact

In this section, the constant speed impacts of wedges with different deadrise angles are studied based on the CFD method. The hydrodynamic forces of the three stages are formulated based on a combination of the results of similarity solution of slamming stage, the CFD results of transition stage and the theoretical results of steady supercavitating flow. The steady supercavitating flow is an approximation of the flow around the wedge at a very large penetration depth and is theoretically formulated in Appendix 7.1 based on the theoretical method of Gurevich [12].

4.1. Pressure distributions of $\beta = 30^\circ$ caused by the constant speed impact

The pressure distributions and free surface of different penetration depths in the transition stage during the water entry of a wedge with $\beta = 30^\circ$ in a constant speed are shown in Fig. 11. It is clearly observed that the high pressure region located at the spray root rapidly vanishes after the spray root leaves the knuckle of the wedge. In the slamming stage, the high pressure region is formed

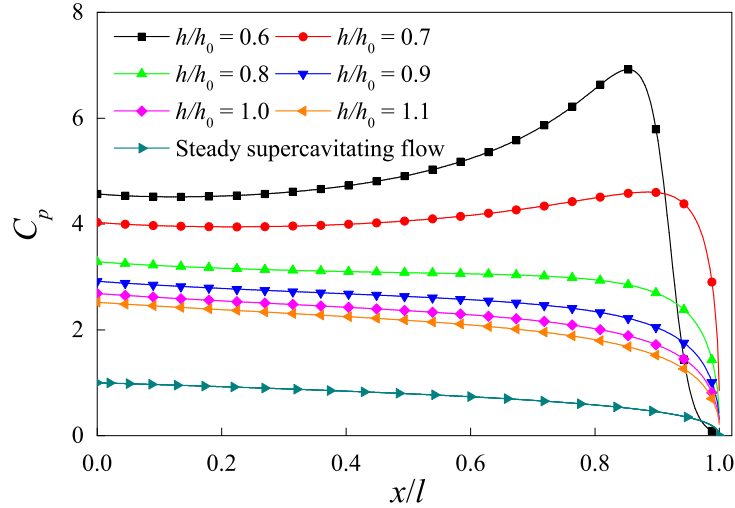


Fig. 12: The pressure distributions on the wedge surface in the transition stage of the water entry of a wedge with $\beta = 30^\circ$ in a constant speed. The result of steady supercavitating flow is calculated by the potential theory in Appendix 7.1.

because the water under the wedge has to accumulate in the spray root and turns into a jet with high speed, as the wetted area of wedge keeps increasing. In the transition stage, the wetted length of the wedge stops increasing and the wall surface of the spray root no longer exists, and thus the high pressure region disappears. Fig. 12 shows the pressure distributions on the wedge surface. With the increasing penetration depth, the pressure on the whole wedge surface decreases and finally approaches the distribution of steady supercavitating flow. It is difficult to figure out the way how the pressure drops from the original distribution of slamming stage. In this paper, we focus on the formulation of the force and expect to find a general expression of slamming and transition stages .

4.2. Hydrodynamic force caused by the constant speed impact

Figure 13 (a) shows the slamming coefficient C_{s0} of different deadrise angles varying from 25° to 45° . The C_{s0} of a single β increases linearly to the maximum C_{\max} and declines to a steady value $C_{s\infty}$. The $C_{s\infty}$ of different deadrise angles

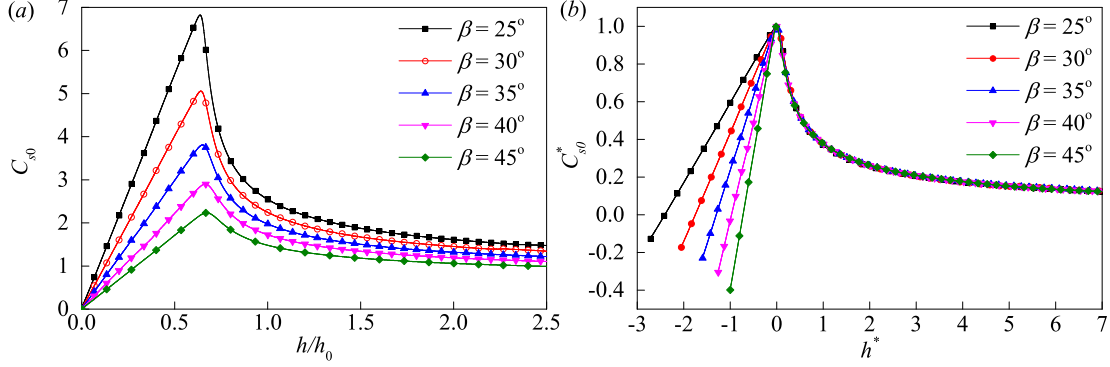


Fig. 13: The slamming coefficient C_{s0} (a) and the new variables C_{s0}^* (b) of different deadrise angles varying from 25° to 45° calculated by the CFD method.

are shown in Fig. 32 in Appendix 7.1, which is calculated by a potential theory [12]. In order to formulate the slamming coefficient C_{s0} in the transition stage, new variables are adopted:

$$h^* = \frac{h - h_2}{h_2} \cot^\lambda \beta, \quad (16)$$

$$C_{s0}^* = \frac{C_{s0} - C_{s\infty}}{C_{s\max} - C_{s\infty}}, \quad (17)$$

where h_2 is the penetration depth corresponding to the maximum slamming coefficient $C_{s\max}$. The new parameter λ is determined by a gradient algorithm enforcing on the following function

$$\eta(\lambda) = \frac{1}{N} \sum_{i=1}^N \sigma_i^2(\lambda), \quad (18)$$

where $\sigma_i(\lambda)$ is the standard deviation of C_{s0}^* between different deadrise angles for the i^{th} node in the range of $h^* \in [0, 7]$ and thereby becomes a function of λ . An uniform distribution with $N=7001$ nodes in the range of $h^* \in [0, 7]$ is adopted, and the initial values are chosen as $\lambda = 1.4$ and 1.35 . After 35 steps, the gradient algorithm is convergent with $\lambda = 1.3075$ ($\Delta\lambda < 1e-6$). The C_{s0}^* of different deadrise angles with $\lambda = 1.3075$ are also shown in Fig. 13 (b), and it can be seen that the C_{s0}^* of different deadrise angles in the transition stage coincide well with each other.

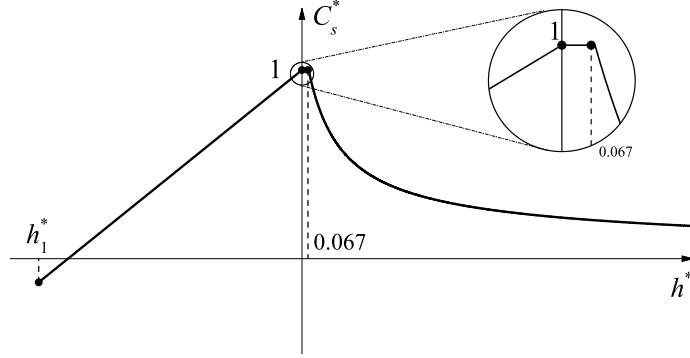


Fig. 14: Description of the formulation for the whole process of water entry.

Owing to the linear increasing slamming coefficient in the slamming stage and the coinciding results in the transition stage, the hydrodynamic force of both the slamming and transition stages of water entry can be formulated as shown in Fig. 14, where the slamming stage is in the range of $[h_1^*, 0]$ and the transition stage is in that of $[0, +\infty]$. The coinciding C_{s0}^* of Fig. 13 (b) in the transition stage is formulated by a rational function in $h^* \in [0, 7]$ based on the mean results of the C_{s0}^* of different deadrise angles

$$C_{s0}^* = \frac{1.539h^* + 2.618}{h^{*2} + 8.081h^* + 2.169}. \quad (19)$$

Due to the fitting errors, C_{s0}^* in Eq. (19) is larger than 1 when $h^* \in [0, 0.067]$. In order to deal with the continuity between Eq. (19) and the linear increasing C_{s0}^* of slamming stage, C_{s0}^* of is approximately as 1 in $h^* \in [0, 0.067]$. The linear increasing C_{s0}^* appears the following form

$$C_{s0}^* = 1 + \frac{\partial C_{s0}^*}{\partial h^*} h^*. \quad (20)$$

By taking the derivative of C_{s0}^* with respect to h^* , the slope of the linear expression of Eq. (20) in $[h_1^*, 0]$ appears to be

$$\frac{dC_{s0}^*}{dh^*} = \frac{k_1 k_2 \tan^3 \beta}{C_{s \max} - C_{s \infty}}, \quad (21)$$

where $k_1 = h_2/h_0$, $k_2 = \frac{dC_{s0}^*}{d(h/h_0)}$. $C_{s \max} = k_1 k_2$ according to the definitions of k_1 and k_2 . Fig. 15 shows the k_1 and k_2 of various deadrise angles from

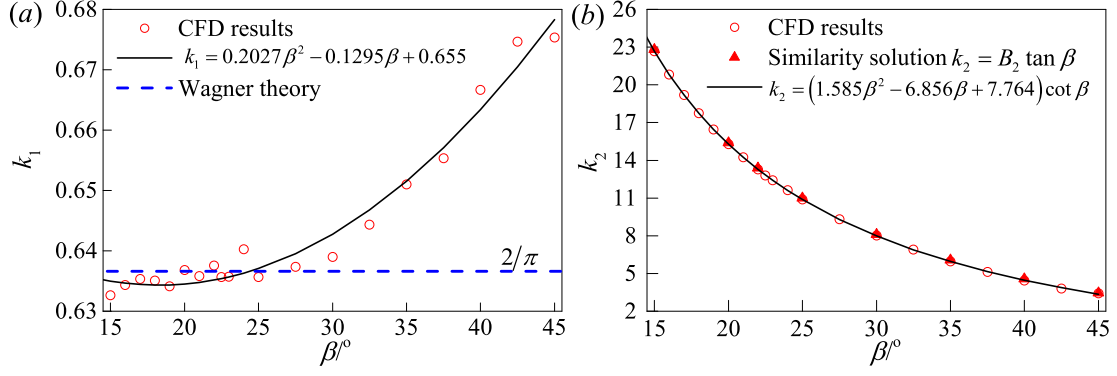


Fig. 15: The k_1 and k_2 of various deadrise angles from 15° to 45° , which are calculated by the present CFD method.

15° to 45° , which are calculated by the present CFD method. In the Wagner theory, $k_1 = 2/\pi$. k_1 from CFD results match $2/\pi$ when $\beta \leq 30^\circ$. Thus, $k_1 = 2/\pi$ can be adopted for small deadrise angle. k_2 appears to be equal to $B_2 \tan \beta$ of the similarity solution [22, 39, 21]. The CFD results of k_2 are in good agreement with the similarity solution. In this paper, the results of k_1 and k_2 for an arbitrarily deadrise angle within the range of $[15^\circ, 45^\circ]$ are given by a least square fitting method (LSF) of a quadratic function $k_1 = 0.2027\beta^2 - 0.1295\beta + 0.655$ and a quadratic function multiplying $\cot \beta$, e.g., $k_2 = (1.585\beta^2 - 6.856\beta + 7.764) \cot \beta$ from the CFD results, and the maximum fitting errors are 0.62% and 1.91% respectively. Therefore

$$C_{s0}^* = \begin{cases} 1 + \frac{\partial C_{s0}^*}{\partial h^*} h^*, & h^* \leq 0 \\ 1, & 0 < h^* \leq 0.067 \\ \frac{1.539h^* + 2.618}{h^{*2} + 8.081h^* + 2.169}, & h^* > 0.067 \end{cases} \quad (22)$$

By combining the Eqs. (16) - (17) and (22), it is possible to find the C_{s0} value and then the hydrodynamic force acting on the wedge surface (half model) for the cases in a constant speed is given

$$F = \frac{1}{2} \rho U_w^2 l C_{s0}. \quad (23)$$

4.3. Comparisons with CFD results

In Sec. 4.2, the formulation of slamming stage in the slamming and transition stages is set up by Eqs. (16)-(17) and (22), and the hydrodynamic force is finally calculated by Eq. (23). The formulation is based on the CFD results in a range of deadrise angles from 15° to 45° . In order to explore its application range of deadrise angles, this section compares the predictions of Eq. (23) and the CFD results in the range of $\beta \in [5^\circ, 70^\circ]$.

For the comparisons in $\beta \in [15^\circ, 45^\circ]$, Fig. 16 shows the comparisons between the predictions of Eq. (23), the modified Wagner's model (MWM) [25] and the CFD method for the cases of $\beta = 15^\circ, 25^\circ$ and 45° . The agreement between the present model and the CFD results is good except that a tiny discrepancy occurs at the maximum C_s for the case of $\beta = 45^\circ$. The MWM can only work in the range of $\beta \in [15^\circ, 35^\circ]$. For the cases of $\beta = 15^\circ$ and 25° , the accuracy of the present model and MWM is close.

The comparisons in the ranges of small and large deadrise angles are also provided in Figs. 17 and 18. The agreement between the predictions of Eq. (23) and the CFD results is generally good, though with some discrepancies. Eq. (23) slightly underestimates the force at a large penetration depth for the case of $\beta = 5^\circ$ and overestimates the forces for the cases of large deadrise angles at an early period of the transition stage. But the agreement becomes better as the penetration depth increases. Therefore, it can be concluded that the present formula can provide accurate predictions for the slamming coefficients of various deadrise angles from 5° to 70° .

Since there exists entrainment of air when the deadrise angle is smaller than 5° [40, 41], the predictions of force without involvement of the effect of air cushion may be inaccurate. Thus, this paper does not consider the validations of a smaller deadrise angle, and $5^\circ \leq \beta \leq 70^\circ$ will be a proper range of deadrise angle for most of the engineering applications.

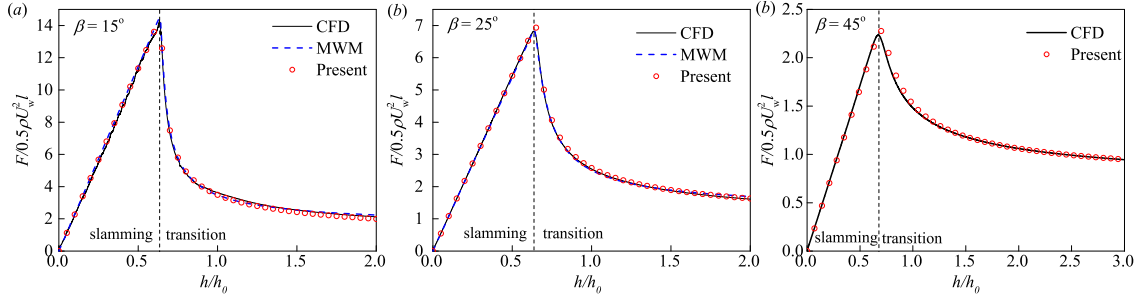


Fig. 16: The comparisons between the predictions of Eq. (23), the modified Wagner's model (MWM) [25] and the CFD method for the water entry of linear wedges with deadrise angles of $\beta = 15^\circ$, 25° and 45° .

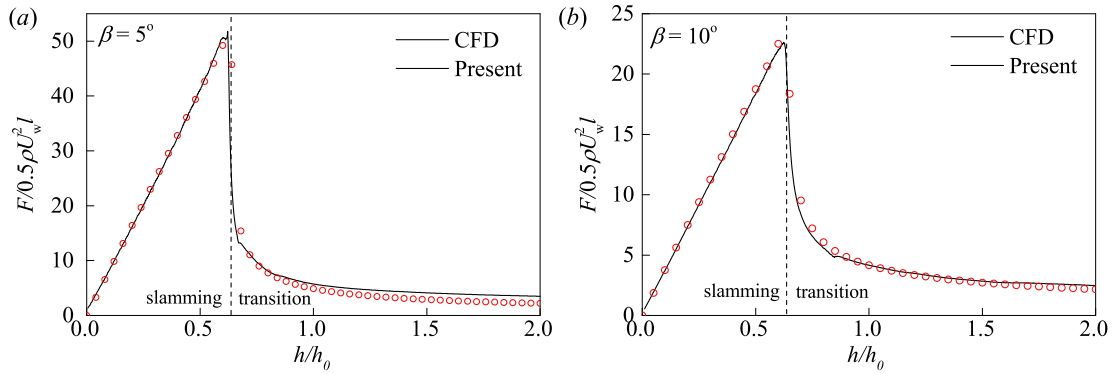


Fig. 17: The comparisons between the predictions of Eq. (23) and the CFD method for water entry of linear wedges with small deadrise angles of $\beta = 5^\circ$ and 10° .

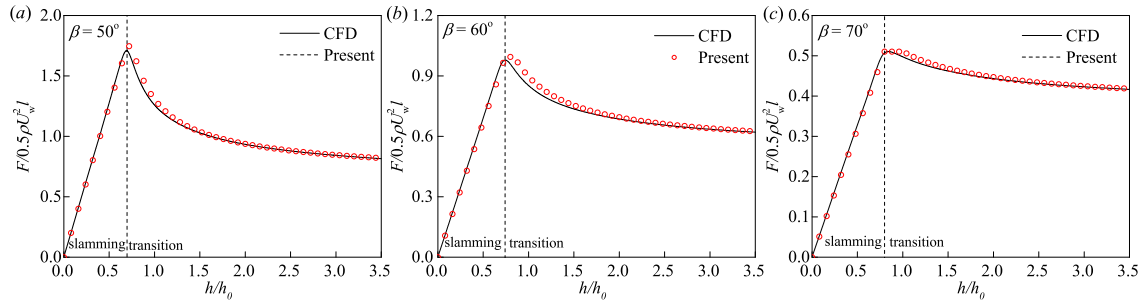


Fig. 18: The comparisons between the predictions of Eq. (23) and the CFD method for water entry of linear wedges with high deadrise angles of $\beta = 50^\circ$, 60° and 70° .

| | β ($^\circ$) | U_0 (m/s) | start time (s) | a_w (m/s 2) |
|--------|----------------------|-------------|----------------|-------------------|
| Case 1 | 30 | 1 | 0.25 | -1 |
| Case 2 | 30 | 1 | 0.25 | -2t+0.2 |
| Case 3 | 30 | 1 | 0.25 | 2t - 2 |
| Case 4 | 15 | 2 | 0.06 | -5 |
| Case 5 | 20 | 1 | 0.15 | -2t + 0.3 |
| Case 6 | 45 | 1 | 0.63 | -0.5t + 0.315 |

Tab. 3: Details of the cases of varying speed impacts in forced motions. The cases remains the impacts in a constant speed of U_0 before the start time and turn into those of a varying speed with the above accelerations after that. Cases 1 and 4 have constant decelerations and the other have linear decelerations.

5. Varying speed impact

In this section, the varying speed impact of a linear wedge is numerically studied by the HBF method described in Sec. 2.2. The varying speed cases are shown in Tab. 3. The wedges have the same half-width of 1m. All the cases start the varying speed motions at the start time in the slamming stage, which makes sure that the impacts in the transition stage are all in varying speed motions. Cases 1 and 4 have constant decelerations and the other have linear decelerations. In the following simulations of HBF, the growth factor of BEM and FEM panels are 1.03 and 1.04 respectively and the ratio between the normal distance between the two side of the jet in proximity of the spray root (to be honest where the jet model start) and the minimum panel size is 2. The pressure distributions and the force acting on the wedge body are discussed by comparing the results of the constant and varying speed impacts. The formulation of the acceleration effect in the transition stage is proposed and the new expression will be validated by numerical and experiment results and compared with other theories.

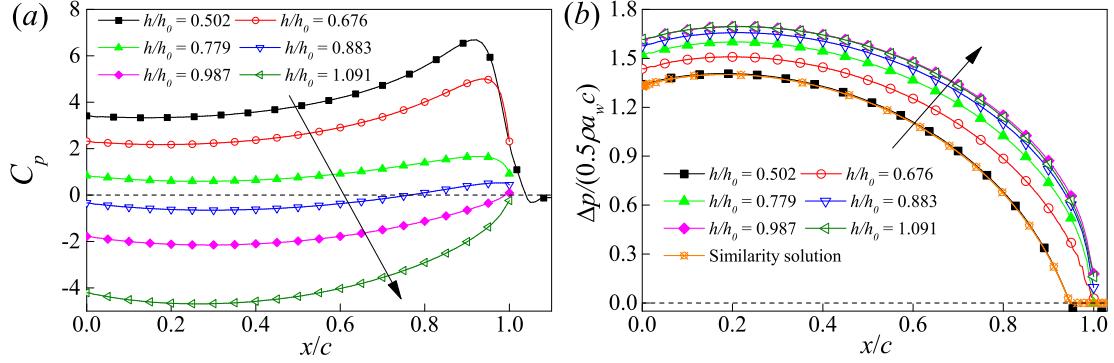


Fig. 19: The C_p distributions on the wedge surface in the transition stage of Case 1 (see Tab. 3) (a) and the distributions of $\Delta p / (0.5\rho_w c)$, where Δp is the difference of the pressure between the varying and constant speed impacts in a same penetration depth and with a same instantaneous speed (b). The result of similarity solution $k_1 \tan \beta (-2\Phi)$ is also given for comparisons[36]. The result of $h/h_0 = 0.502$ remains in the slamming stage.

5.1. Pressure distributions of $\beta = 30^\circ$ caused by the acceleration effect

Figure 19 (a) shows the C_p distributions on the wedge surface in the transition stage of Case 1 (see Tab. 3). For the case of $\beta = 30^\circ$, the transition stage starts at $h/h_0 = 0.639$ and thus the result of $h/h_0 = 0.502$ is still in the slamming stage while the other are in the transition stage. As can be seen in Fig. 19 (a), the C_p distributions along the wedge surface decline with the increasing penetration depth. The reasons of the pressure drop includes two different aspects: the vanishing of high pressure region at spray root (see Sec. 3.1) and the deceleration of wedge. In order to distinguish these two kinds of influence, the pressure is split into two parts: (1) the pressure only related to the constant speed impact $p_0 = 0.5\rho_w U_w^2 C_{p0}$ (see Fig. 12); (2) the pressure changing $\Delta p = p - p_0$ caused by the acceleration of wedge, where p_0 and p are the pressure of the constant and varying speed impacts respectively in a same penetration depth and with a same instantaneous speed. Fig. 19 (b) shows the distributions of $\Delta p / (0.5\rho_w c)$, where the effective wetted length (half length) is $c = \min \{h \cot \beta / k_1, l\}$. The $\Delta p / (0.5\rho_w c)$ of different penetration depths show similar distributions and have a small increase along the whole wedge

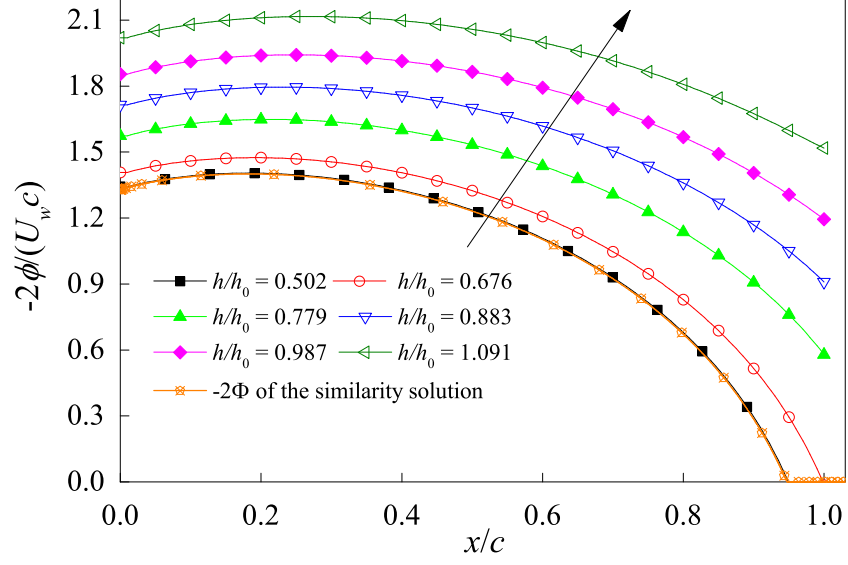


Fig. 20: The dimensionless velocity potential $-2\phi/(U_w c)$ on the wedge surface of Case 1 in the transition stage. The result of $h/h_0 = 0.502$ remains in the slamming stage.

surface with the increasing penetration depth. The result of similarity solution $k_1 \tan \beta(-2\Phi)$ [36] in the slamming stage is well consistent with the result $h/h_0 = 0.502$ in the slamming stage. It can be concluded that the distribution of $\Delta p/(0.5\rho a_w c)$ remains as $k_1 \tan \beta(-2\Phi)$ in the slamming stage and then has a small increase in the transition stage. The results become steady as the penetration depth continues to increase. The small increase pressure will also result in the small increase of slamming coefficient, which will be further discussed in Sec. 5.2.

From the studies of slamming stage [36, 21], the pressure changing caused by the acceleration of wedge can be quantified by the dimensionless velocity potential -2Φ . Fig. 20 shows the dimensionless velocity potential $-2\phi/(U_w c)$ (a similar dimensionless variable like -2Φ) on the wedge surface of Case 1 in the transition stage. The $-2\phi/(U_w c)$ distribution of $h/h_0 = 0.502$ is identical to -2Φ of the similarity solution [21] since it still remains in the slamming stage.

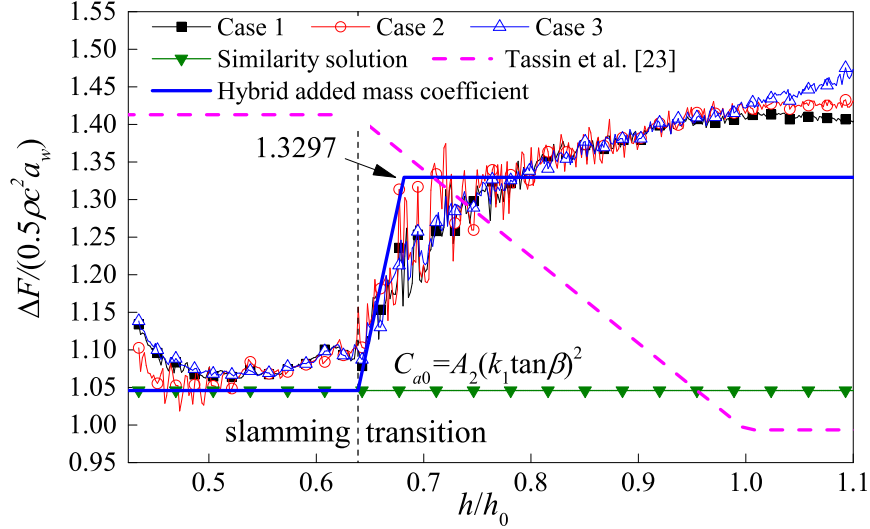


Fig. 21: The time histories of $\Delta F/(0.5\rho c^2 a_w)$ of different prescribed speeds (Case 1, Case 2 and Case 3 in Tab. 3), where ΔF is difference of force between the varying and constant speed impacts in a same penetration depth and with a same instantaneous speeds. The results of $C_{a0} = A_2(k_1 \tan \beta)^2$ from the similarity solution [36] and Eq. (26) from Tassin et al. [23] are also given for comparisons.

The other distributions show large differences with -2Φ of the similarity solution and the $\Delta p/(0.5\rho a_w c)$ distributions in Fig. 19 (b). It can be concluded that the pressure changing caused by the acceleration of wedge can not be quantified by the velocity potential in the transition stage as it does in the slamming stage. Although the $\Delta p/(0.5\rho a_w c)$ distributions have a similar distribution and small increase as the penetration depth increases, there is still some challenging problems to formulate the pressure changing caused by the acceleration effect. In this paper, we focus on the formulation of the hydrodynamic force caused by the acceleration effect and hope to find an effective method to formulate the hydrodynamic force caused by the acceleration effect.

5.2. Hydrodynamic force caused by the acceleration effect

Similar to the pressure distribution on the wedge surface, the force can also be divided into two part: (1) the force caused by the constant speed impact

$F_0 = 0.5\rho U_w^2 l C_{s0}$, where C_{s0} can be given by Eqs. (16) - (17) and (22); (2) the force caused by the acceleration effect $\Delta F = F - F_0$, where F_0 and F are the forces of constant and varying speed impacts respectively in a same penetration depth and with a same instantaneous speed. Fig. 21 shows the $\Delta F/(0.5\rho c^2 a_w)$ of different prescribed speeds (Cases 1,2 and 3 in Tab. 3). All of the cases are decelerating with different decelerations. Case 1 has a constant deceleration, Case 2 has an increasing deceleration and Case 3 has a decreasing deceleration. The $\Delta F/(0.5\rho c^2 a_w)$ show good consistence between different cases in the transition stage of $h/h_0 \in [0.639 \ 1.0]$, though with some numerical fluctuations. Therefore, $C_a = \Delta F/(0.5\rho c^2 a_w)$ is defined as an added mass coefficient, and independent of a_w in $h/h_0 \in [0.639 \ 1.0]$. It can be concluded that the effects of acceleration on the hydrodynamic force have a fixed pattern in the transition stage as it does in the slamming stage [21]. In the slamming stage, the acceleration effect on the hydrodynamic force is given as $\Delta F = \rho A_2 a_w h^2$ from the similarity solution [36], indicating an added mass coefficient $C_{a0} = A_2(k_1 \tan \beta)^2$. The C_a in the slamming stage can be given as $C_{a0} = 1.0459$, and in the transition stage, C_a has an averaged result of 1.3297 in $h/h_0 \in [0.639 \ 1.0]$, which is $\xi = 27.13\%$ larger than the result of similarity solution C_{a0} . In this paper, a hybrid added mass coefficient is adopted to formulate the acceleration effect corresponding to Eq. (22)

$$C_a = \begin{cases} C_{a0}, & h^* \leq 0 \\ (1 + \xi h^*/0.067)C_{a0}, & 0 < h^* \leq 0.067 \\ (1 + \xi)C_{a0} & h^* > 0.067 \end{cases} \quad (24)$$

The results of $h^* \in [0, 0.067]$ are given by a linear distribution from C_{a0} to $(1 + \xi)C_{a0}$. For the case of $\beta = 30^\circ$, the approximation of C_a in the transition stage is summarized from the HBF results of $h/h_0 \in [0.639, 1.0]$, corresponding to $h^* \in [0, 1.1586]$. However, further validations of Eq. (24) by the numerical results in Sec. 5.3 indicates that Eq. (24) can work in a larger range of h^* and deadrise angles. Therefore, for the water entry of linear wedges with an acceleration, the hydrodynamic force can be predicted by Eq. (24) together with Eqs. (16) - (17) and (22), and the final expression of the force (half model) has the following

form:

$$F = \frac{1}{2}\rho U_w^2 l C_{s0} + \frac{1}{2}\rho c^2 a_w C_a, \quad (25)$$

where $c = \min \{h \cot \beta / k_1, l\}$.

In the linear FBC of Tassin et al. [23] based on MLM, the acceleration effect was addressed by the following form of C_a of in the slamming and transition stages

$$C_a = \begin{cases} \frac{\pi}{2} + \left(1 - \frac{4}{\pi}\right) \tan \beta, & \frac{h}{h_0} \leq \frac{2}{\pi} \\ \frac{\pi}{2} + \left(1 - \frac{2h}{h_0}\right) \tan \beta, & \frac{2}{\pi} < \frac{h}{h_0} \leq 1 \\ \frac{\pi}{2} - \tan \beta. & \frac{h}{h_0} > 1 \end{cases} \quad (26)$$

As can be seen in Fig. 21, the present model has a different C_a from that of Tassin et al. [23].

5.3. Validations by numerical and experiment results

Figure 22 shows the comparisons of the forces acting on the wedge surface between the present predictions and the HBF results for Case 1, 2 and 3. The results of Eq. (23) only include the effect of constant speed impact while those of Eqs. (25) include the effect of constant speed impact and the acceleration effect. The predictions of Eqs. (25) are in good agreement with the HBF results, while those of Eqs. (23) show much discrepancies with the HBF results. Fig. 23 shows comparisons for Case 4, 5 and 6 of different deadrise angles and different ways of decelerations. The same C_a correction of $\xi = 27.13\%$ is adopted for the cases of different deadrise angles, and the good agreement is also obtained. It indicates that the C_a correction of $\xi = 27.13\%$ also works for other deadrise angles.

To explore the application ranges of deadrise angles and of different ways of wedge motions for the present model, Fig. 24 shows the comparisons of the forces acting on the wedge surface between the present predictions and the CFD results for the freefall cases of (a) $\beta = 5^\circ$ and $\beta = 70^\circ$. The wedges are in freefall motions with masses of $m = 1.5\rho l^2$. For the small and high deadrise angles, the present model can provide good predictions for the hydrodynamic forces, even for the freefall motions where the acceleration of wedge is unknown before the predictions.

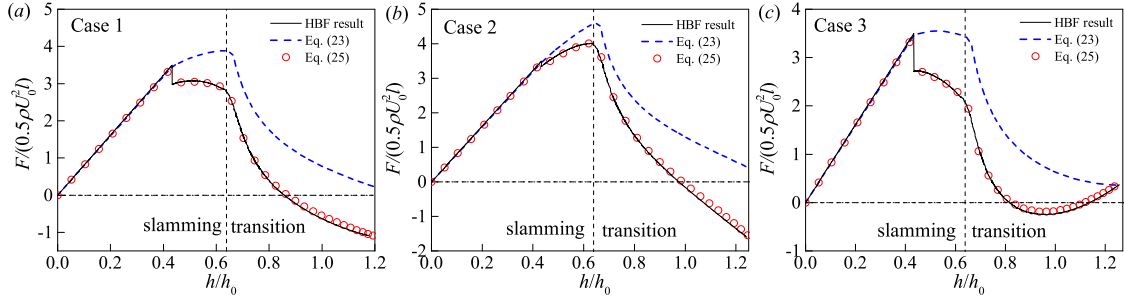


Fig. 22: The comparisons of the forces acting on the wedge surface between the present predictions and the HBF results for Case 1, 2 and 3.

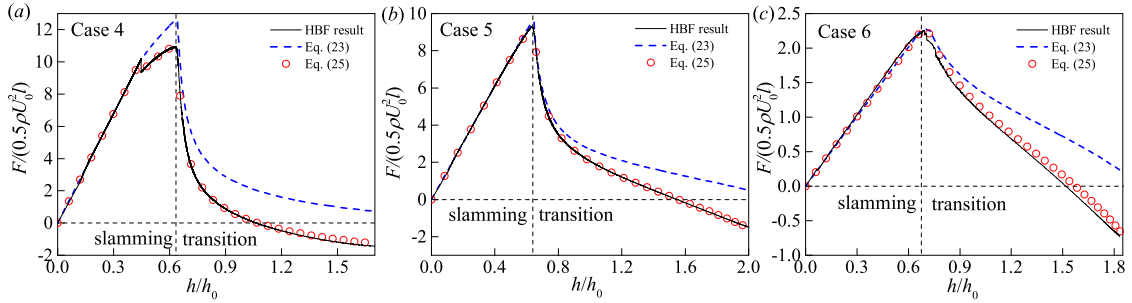


Fig. 23: The comparisons of the forces acting on the wedge surface between the present predictions and the HBF results for Case 4, 5 and 6.

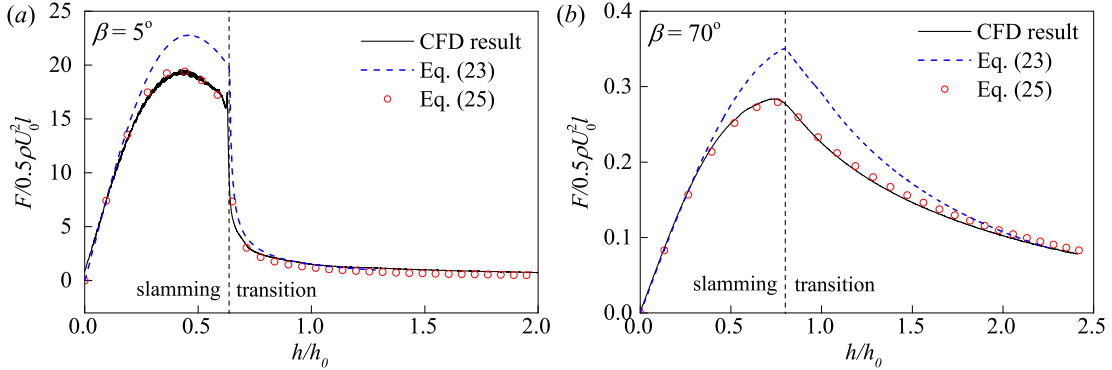


Fig. 24: The comparisons of the forces acting on the wedge surface between the present predictions and the CFD results for the freefall cases of (a) $\beta = 5^\circ$ and (b) $\beta = 70^\circ$ with masses of $m = 1.5\rho l^2$.

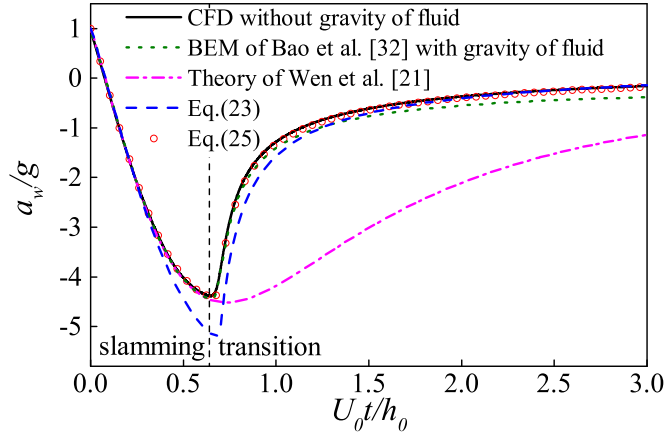


Fig. 25: The comparisons of the predictions of accelerations of wedge with $\beta = 30^\circ$ between the CFD without gravity of fluid, BEM of Bao et al. [32] with gravity of fluid, theory of Wen et al. [21] without considering the transition stage, Eqs. (23) and (25) during the water entry in freefall motion.

The case in Fig. 10 is also used for a validation for the present model. Fig. 25 shows the comparisons of the predictions of accelerations of wedge with $\beta = 30^\circ$ between the CFD without gravity of fluid, BEM of Bao et al. [32] with gravity of fluid, theory of Wen et al. [21] without considering the transition stage, Eq. (23) and Eq. (25) during the water entry in freefall motion. The agreement between the CFD result and the present model with acceleration effect, e.g., Eq. (25), is good in both slamming and transition stages, while the theory of approximate solution without considering the transition stage [21] can only address the slamming stage. The present model without acceleration effect, e.g., Eq. (23), also shows large differences compared with the CFD result. The gravity effect has small influence on the hydrodynamic force in the transition stage for the cases of $Fr = 1.9587$. For the high speed impact of higher Fr , the gravity of fluid can be neglected and the present model will have better predictions.

A comparison of the forces between an experimental test of Zhao et al. [13] and the present model is shown in Fig. 26. The case is a three-dimensional water

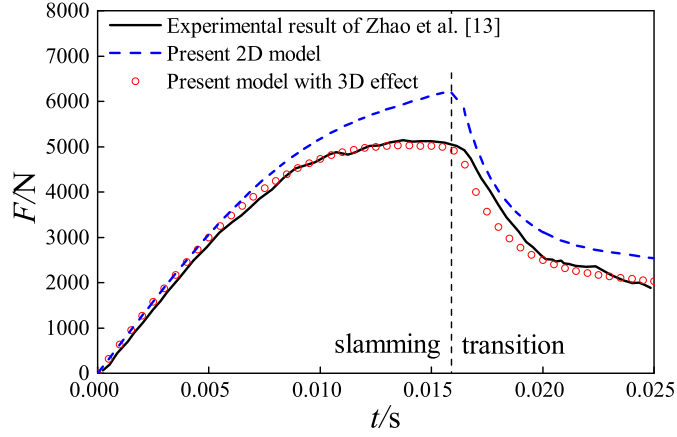


Fig. 26: The comparisons between the present predictions of forces and the experimental result of Zhao et al. [13] for the water entry of a wedge of $\beta = 30^\circ$. The vertical velocity of the wedge is given by the experimental result of an optical sensor. The force coefficient of 3D effect is approximately formulated as a parabolic $f_{3D} = 1 - 0.80(c/l)^2$ by using Meyerhoff's results [42].

entry with deadrise angle of $\beta = 30^\circ$. The half width of wedge is $l = 0.25$ m and the thickness is $L = 1$ m. The vertical speed of the wedge is given by the experimental result of an optical sensor. The acceleration of wedge is given by the derivative of vertical speed. The present 2D model has large discrepancies compared with the experimental result. As Zhao et al. indicated, the reason is due to the three dimensional (3D) effect and the force should be corrected by a force coefficient f_{3D} (a function of c/L). They used Meyerhoff's results [42] of $f_{3D}(0.25) = 0.95$, $f_{3D}(0.4) = 0.87$, $f_{3D}(0.5) = 0.8$ from the added masses of thin rectangular plates with a generalization of Wagner theory to formulate the 3D effect. In this paper, a parabolic $f_{3D} = 1 - 0.80(c/L)^2$ is approximately formulated by fitting from the above results. After using the 3D correction, the present model with 3D effect can predict the force of the experimental test.

To sum up, Eq. (25) together with Eqs. (16), (17), Eq. (24) and (22) can be used for both the predictions of hydrodynamic force in slamming and transition stages for the water entry of wedges with different deadrise angles in constant

| Model | γ | C_{const} | C_a |
|-----------------------------|-----------------------|--|---|
| Von Karman [4] | 1 | π | 1 |
| Wagner's original model [5] | $\frac{\pi}{2}$ | $\frac{\pi^3}{4}$ | $\frac{\pi}{2}$ |
| Wagner's new model [5] | $\frac{\pi}{2}$ | $\pi \left(\frac{\pi}{2\beta} - 1 \right)^2 \tan^2 \beta$ | $\frac{\pi}{2}$ |
| Faltinsen [17] | $\frac{\pi}{2}$ | $\frac{\pi^3}{4} \left(1 - \frac{\beta}{2\pi} \right)^2$ | $\frac{\pi}{2} \left(1 - \frac{\beta}{2\pi} \right)^2$ |
| Mei et al. [19] | γ_{Mei} | $B_{2\text{Mei}} \tan^2 \beta$ | $A_{2\text{Mei}} (\tan \beta / \gamma_{\text{Mei}})^2$ |
| Tassin et al. [23] | $\frac{\pi}{2}$ | C_{Korobkin} | $\frac{\pi}{2} - \left(\frac{4}{\pi} - 1 \right) \tan \beta$ |
| Present model | $\frac{1}{k_1}$ | $B_2 \tan^2 \beta$ | $A_2 (k_1 \tan \beta)^2$ |

Tab. 4: The correction factor γ of the wetted length, the dimensionless coefficient of constant speed impact C_{const} and the added mass coefficient C_a of slamming stage for different theories.

and varying speeds.

5.4. Comparisons with other theories

For the slamming stage, the traditional added mass methods have the forms of added mass and the hydrodynamic force (half model)

$$m_0 = \frac{1}{2} \rho c^2 C_a, \quad (27)$$

$$F = \frac{d(m_0 U_w)}{dt} = \frac{1}{2} \rho U_w^2 h \cot^2 \beta C_{\text{const}} + \frac{1}{2} \rho c^2 a_w C_a, \quad (28)$$

where $c = \gamma h \cot \beta$ for the traditional methods. Tab. 4 shows the correction factor γ of the wetted length, the dimensionless coefficient of constant speed impact C_{const} and the added mass coefficient C_a of slamming stage for different theories [4, 5, 17, 19, 23]. The Wagner's new model [5] was proposed to improve the predictions of forces of constant speed impact for different deadrise angles, but the acceleration term remained unchanged. γ_{Mei} can be found in Refs. [19, 21]. $B_{2\text{Mei}}$ and $A_{2\text{Mei}}$ are calculated by direct pressure and velocity potential integrations of Mei et al.'s model [19]. C_{Korobkin} is from the theoretical results of Korobkin [20]. B_2 and A_2 of the present model were calculated from the similarity solution [22], and the results are shown in Ref. [21].

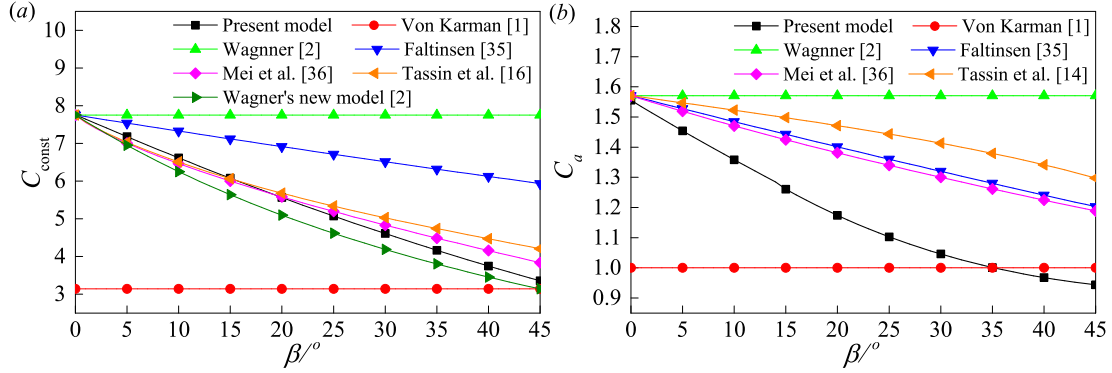


Fig. 27: The comparisons of the dimensionless coefficient of (a) constant speed impact C_{const} and (b) added mass coefficient C_a of the slamming stage between the present model and other theories [4, 5, 17, 19, 23].

In early researches of Refs. [4, 5, 17, 19, 20] for the slamming stage, the hydrodynamic force of constant speed impact received the most attention and the researchers proposed their models by comparing the results of similarity solution [22, 16] to correct the underestimated results of Von Karman [4] and overestimated results of Wagner's original model [5], as shown in Fig. 27 (a). The models of Mei et al. [19], Tassin et al. [23] and Wagner's new model [5] have been approximately close to the results of similarity solution, but these models actually violate the framework of added mass methods. Their C_{const} are no longer $2C_a\gamma^2$, which are different from the models of Von Karman [4], Wagner [5] (original model) and Faltinsen [17]. Although these models [19, 23, 5] brought good predictions for the constant speed impact, they still can not properly model the acceleration effect, as shown in Fig. 27 (b). The Faltinsen's model cannot properly address both the constant speed impact and acceleration effect. The present model formulates the models of constant speed impact and acceleration effect directly from the approximate solution [21] based on the similarity solution of Dobrovolskaya [22], regardless of the framework of added mass methods and the consistency of C_{const} and C_a . The validations by numerical results in Ref. [21] and Figs. 22 and 23 have completely verified the present model.

For the transition stage, Tassin et al.'s model [23], the MWM of Wen et al. [25] and the present model can address both the slamming and transition stages, while the models of Ref. [4, 5, 17, 19] can only work in the slamming stage. Wen et al. had greatly improved the predictions of hydrodynamic forces for the constant speed impact in the range of $\beta \in [15^\circ, 35^\circ]$ compared with the linear FBC of Tassin et al. and the improved model of zero pressure condition [18, 23]. The accuracy of present model is close to Wen et al.'s MWM, but with a much larger range of deadrise angle. Besides, the acceleration effect in the transition stage is missing in MWM. Tassin et al.'s model provided the formulation of acceleration effect and the C_a is given by Eq. (26). The comparison of C_a of $\beta = 30^\circ$ between the present model and Tassin et al.'s model is shown in Fig. 27 (b). In contrast to an increase of C_a in the transition stage, the C_a of Tassin et al.'s model declines and finally reaches a constant value lower than C_{a0} , which is inconsistent with the HBF results in Fig. 27 (b).

In general, we rewrite the formula of hydrodynamic force and extend it to the transition stage for the constant and varying speed impacts. Although the present model is more sophisticated, it works better than the traditional added mass methods and the asymptotic theories and can work in a larger range of deadrise angle.

6. Conclusions

In this paper, the transition stage of the water entry of a linear wedge with constant and varying speeds is numerically studied by FVM with VOF and HBF. The hydrodynamic force acting on the wedge is formulated by a combination of the numerical results and theoretical results of the steady supercavitating flow. The fluid is assumed to be incompressible, inviscid, weightless and with negligible surface tension, and the flow is irrotational for the high speed impact. For the constant speed impact, the similitude of the slamming coefficients of different deadrise angles in the transition stage is found by scaling the difference between the maximum values in the slamming stage and the results of steady

supercavitating flow. The formulation of the hydrodynamic force is conducted based on the similitude of the declining forces in the transition stage together with the linear increasing results in the slamming stage. For the varying speed impact, the acceleration effects on the pressure distribution and force acting on the wedge surface are revealed. The hydrodynamic force caused by the acceleration effect in the transition stage is formulated by an added mass coefficient with an averaged increase of 27.13% compared with that of slamming stage. A general expression of the slamming coefficient with the deadrise angles from 5° to 70° in both the slamming and transition stages is thus proposed for the constant and varying speed impacts, and its predictions are in good agreement with the numerical and experiment results. Thus, it can be treated as a 2D water entry model the 2.5D method being used on the take-off and water landing of seaplanes, and for the strip theory or 2D+t theory being used on the hull slamming.

Acknowledgements

This work was partially supported by the National Natural Science Foundation of China (No. 12072014 and No. 11721202).

7. Appendix

7.1. The theory of steady supercavitating flow

The water entry in the infinite penetration depth becomes a steady supercavitating flow with an incoming current with velocity v_0 . The theory can be extended from the water entry on a plate by the theory of Gurevich [12]. The free surface CD and C'D' of impact flow is shown in Fig. 28 after the solution is solved. The direction of incoming flow is upward and the stream-function on the streamline passing A is 0. The velocity potential at A is chosen as 0. A parameter plane τ mapping to the geometry in Fig. 28 is shown in Fig. 29 and thus the complex velocity potential of impact flow can be calculated as

$$w = \phi_0 \tau^2, \quad (29)$$

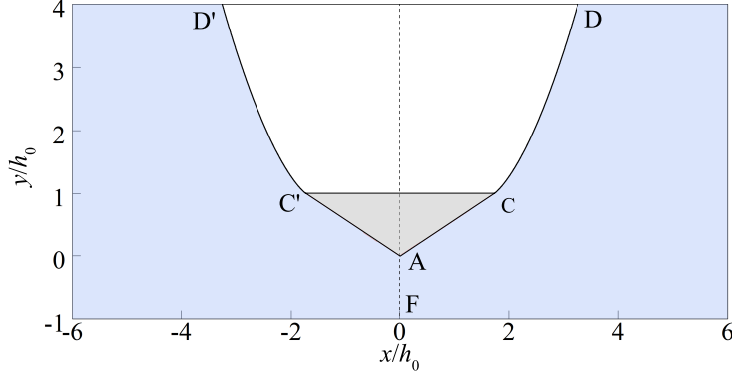


Fig. 28: Free surface of the steady supercavitating flow for a 2D wedge of $\beta = 30^\circ$.

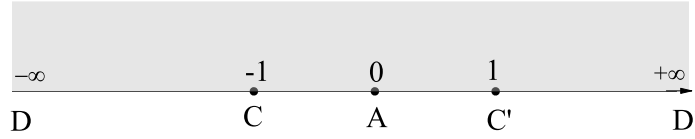


Fig. 29: The τ plane of the steady supercavitating flow.

where ϕ_0 is the velocity potential at C and C' . Another parameter plane $\omega = v_0 \frac{dz}{dw} = v_0 e^{i\theta} / v$ (i being the imaginary unit) mapping to the velocity is shown in Fig. 30 and can be formulated by the Schwarz-Christoffel formula as

$$\omega(\tau) = \left(1 - \frac{2\beta}{\pi}\right) \ln \left(\sqrt{1 - 1/\tau^2} + \frac{i}{\tau} \right) + i\frac{\pi}{2}. \quad (30)$$

The complex coordinate can be derived

$$z = \int \frac{dz}{dw} \frac{dw}{d\tau} d\tau = \frac{2\phi_0}{v_0} i \int \left(\sqrt{1 - 1/\tau^2} + \frac{i}{\tau} \right)^{1 - \frac{2\beta}{\pi}} \tau d\tau. \quad (31)$$

By considering the distance from A to C , the velocity potential at C and C' can be determined

$$\frac{2\phi_0}{v_0} = \frac{l}{A \cos \beta}, \quad (32)$$

where

$$A = \int_0^1 \left(\frac{1 + \sqrt{1 - \tau^2}}{\tau} \right)^{1 - \frac{2\beta}{\pi}} \tau d\tau \quad (33)$$

Therefore, the x on AC is given as

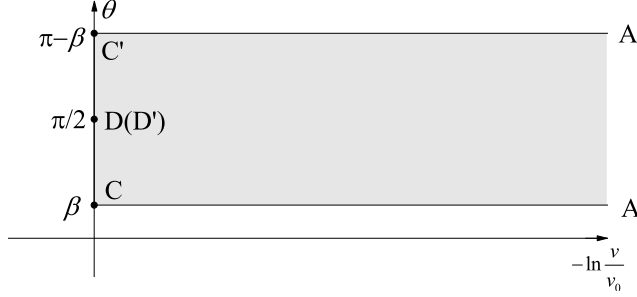


Fig. 30: The ω plane of the steady supercavitating flow.

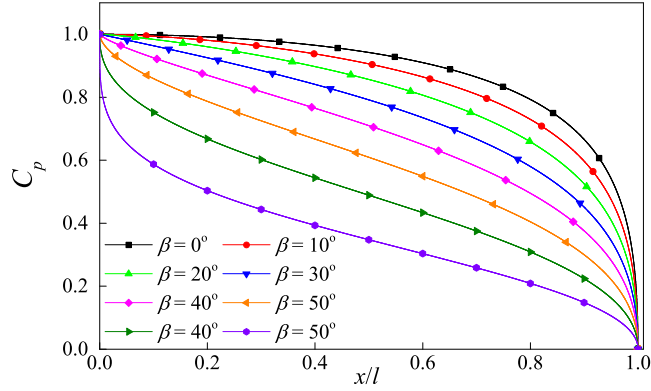


Fig. 31: The C_p distributions of different deadrise angles for the steady supercavitating flow.

$$x(\tau) = \frac{l}{A} \int_0^\tau \left(\frac{1 + \sqrt{1 - \tau^2}}{\tau} \right)^{1 - \frac{2\beta}{\pi}} \tau d\tau, \quad (34)$$

and the velocity on AC is

$$v = v_0 \left(\frac{1 - \sqrt{1 - \tau^2}}{\tau} \right)^{1 - \frac{2\beta}{\pi}} \quad (35)$$

The pressure coefficient C_p has the form

$$C_p = 1 - \left(\frac{1 - \sqrt{1 - \tau^2}}{\tau} \right)^{2(1 - \frac{2\beta}{\pi})}. \quad (36)$$

The C_p distributions of different deadrise angles β are shown in Fig. 31. The C_p is 1 at the stagnation A and 0 at the separation C for a steady supercavitating flow. The free surface profile in Fig. 28 is given by the following x and y

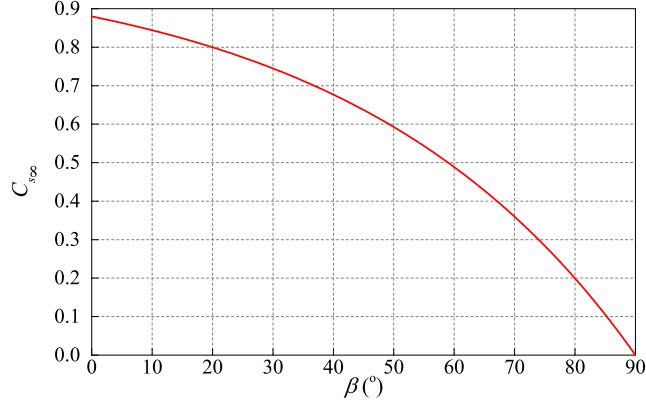


Fig. 32: The slamming coefficient $C_{s\infty}$ of the steady supercavitating flow.

expressions

$$x(\tau) = l - \frac{l}{A \cos \beta} \operatorname{Re} \left[i \int_1^\tau \left(\sqrt{1 - 1/\tau^2} + \frac{i}{\tau} \right)^{1 - \frac{2\beta}{\pi}} \tau d\tau \right], \quad (37)$$

$$y(\tau) = l \tan \beta + \frac{l}{A \cos \beta} \operatorname{Im} \left[i \int_1^\tau \left(\sqrt{1 - 1/\tau^2} + \frac{i}{\tau} \right)^{1 - \frac{2\beta}{\pi}} \tau d\tau \right]. \quad (38)$$

The force acting on the wedges is calculated by integrating the pressure with the C_p expression Eq. (36). The slamming coefficient $C_{s\infty}$ of different deadrise angles is shown in Fig. 32. The result of $\beta = 0$ is equal to 0.88, which is consistent with that of water entry on a plate derived by Gurevich [12]. The $C_{s\infty}$ decreases with the increasing deadrise angle and reaches 0 at $\beta = 90^\circ$.

Korvin-Kroukovsky and Chabrow [11] in 1948 had already presented the calculation of pressure distribution on the wedge surface. The present theory is consistent with their model.

References

References

- [1] W. L. Mayo, Analysis and modification of theory for impact of seaplanes on water, Tech. rep., National Advisory Council for Aeronautics (NACA)

- Technical Note 1008, Langley Field, VA, USA (1945).
- [2] B. Milwitzky, A generalized theoretical and experimental investigation of the motions and hydrodynamic loads experienced by v-bottom seaplanes during step-landing impacts, Tech. rep., National Advisory Council for Aeronautics (NACA) Technical Note 1516, Langley Field, VA, USA (1948).
 - [3] R. F. Smiley, A semiempirical procedure for computing the water-pressure distribution on flat and v-bottom prismatic surfaces during impact or planing, Tech. rep., National Advisory Council for Aeronautics (NACA) Technical Note 2583 (1951).
 - [4] T. Von Karman, The impact on seaplane floats during landing, Tech. rep., National Advisory Council for Aeronautics (NACA) Technical Note 321, Langley Field, VA, USA (1929).
 - [5] H. Wagner, Über stoß- und gleitvorgänge an der oberfläche von flüssigkeiten, ZAMM-Journal of Applied Mathematics and Mechanics/Zeitschrift für Angewandte Mathematik und Mechanik 12 (4) (1932) 193–215.
 - [6] X. Duan, W. Sun, C. Chen, M. Wei, Y. Yang, Numerical investigation of the porpoising motion of a seaplane planing on water with high speeds, Aerospace Science and Technology 84 (2018) 980–994. doi:10.1016/j.ast.2018.11.037.
 - [7] B. Guo, P. Liu, Q. Qu, J. Wang, Effect of pitch angle on initial stage of a transport airplane ditching, Chinese Journal of Aeronautics 26 (1) (2013) 17–26.
 - [8] Q. Qu, M. Hu, H. Guo, P. Liu, R. K. Agarwal, Study of ditching characteristics of transport aircraft by global moving mesh method, Journal of Aircraft 52 (5) (2015) 1550–1558.
 - [9] D. Savitsky, Hydrodynamic design of planing hulls, Marine Technology 1.

- [10] D. Savitsky, M. DeLorme, R. Datla, Inclusion of whisker spray drag in performance prediction method for high-speed planing hulls, *Marine Technology* 44 (2007) 35–56.
- [11] B. Korvin-Kroukovsky, F. R. Chabrow, The discontinuous fluid flow past an immersed wedge, Tech. rep., Stevens Institute of Technology, Hoboken New Jersey, Davidson Laboratory, Experimental Towing tank, Report SIT-DL-48-9-334 (Oct. 1948).
- [12] M. Gurevich, Chapter I - Introduction to the theory of jets in plane steady flows, in: *The Theory of Jets in an Ideal Fluid*, Vol. 93 of *International Series of Monographs on Pure and Applied Mathematics*, Pergamon, 1966, pp. 1 – 36. doi:<https://doi.org/10.1016/B978-0-08-011706-5.50004-2>.
- [13] R. Zhao, O. M. Faltinsen, J. Aarsnes, Water entry of arbitrary two-dimensional sections with and without flow separation, in: *Proceedings of the 21st Symposium on Naval Hydrodynamics*, National Academy Press, Trondheim, Norway, pp. 408–423.
- [14] H. Sun, O. M. Faltinsen, The influence of gravity on the performance of planing vessels in calm water, *Journal of Engineering Mathematics* 58 (1-4) (2007) 91–107.
- [15] H. Sun, O. M. Faltinsen, Hydrodynamic forces on a semi-displacement ship at high speed, *Applied Ocean Research* 34 (none) (2012) 68–77.
- [16] R. Zhao, O. M. Faltinsen, Water entry of two-dimensional bodies, *Journal of Fluid Mechanics* 246 (1991) 593–612.
- [17] O. M. Faltinsen, *Sea loads on ships and offshore structures*, Vol. 1, Cambridge university press, 1993.
- [18] G. V. Logvinovich, *Hydrodynamics of free-boundary flows*, Israel Program for Scientific Translations, Jerusalem, 1972.

- [19] X. Mei, Y. Liu, D. K. Yue, On the water impact of general two-dimensional sections, *Applied Ocean Research* 21 (1) (1999) 1–15.
- [20] A. Korobkin, Analytical models of water impact, *European Journal of Applied Mathematics* 15 (6) (2004) 821–838.
- [21] X. Wen, P. Liu, Q. Qu, T. Hu, Numerical and theoretical study on the varying speed impact of wedge bodies on a water surface, *ASME Journal of Fluids Engineering* 143 (1) (2021) 011201. doi:10.1115/1.4048132.
- [22] Z. Dobrovolskaya, On some problems of similarity flow of fluid with a free surface, *Journal of Fluid Mechanics* 36 (4) (1969) 805–829.
- [23] A. Tassin, A. A. Korobkin, M. J. Cooker, On analytical models of vertical water entry of a symmetric body with separation and cavity initiation, *Applied Ocean Research* 48 (2014) 33–41.
- [24] A. Iafrati, D. Battistin, Hydrodynamics of water entry in presence of flow separation from chines, in: *Proceedings of the 8th International Conference on Numerical Ship Hydrodynamics*, Busan, Korea, 2003.
- [25] X. Wen, Q. Qu, P. Liu, S. Ding, Theoretical study on slamming and transition stages of normal impacts of symmetrical bodies on calm and wavy water surfaces, *Applied Ocean Research* 119 (2022) 102986. doi:https://doi.org/10.1016/j.apor.2021.102986.
- [26] Y. A. Semenov, G. X. Wu, Water entry of an expanding wedge/plate with flow detachment, *Journal of Fluid Mechanics* 797 (2016) 322–344.
- [27] Y. A. Semenov, A. Iafrati, On the nonlinear water entry problem of asymmetric wedges, *Journal of Fluid Mechanics* 547 (2006) 231–256.
- [28] Y. A. Semenov, G. X. Wu, Liquid impact on a permeable solid body, *European Journal of Mechanics-B/Fluids* 57 (2016) 22–30.

- [29] D. Battistin, A. Iafrati, Hydrodynamic loads during water entry of two-dimensional and axisymmetric bodies, *Journal of Fluids & Structures* 17 (5) (2003) 643–664.
- [30] A. Del Buono, G. Bernardini, A. Tassin, A. Iafrati, Water entry and exit of 2d and axisymmetric bodies, *Journal of Fluids and Structures* 103 (2021) 103269.
- [31] J. Wang, O. M. Faltinsen, Numerical investigation of air cavity formation during the high-speed vertical water entry of wedges, *Journal of offshore mechanics and arctic engineering* 135 (1) (2013) 011101. doi:10.1115/1.4006760.
- [32] C. M. Bao, G. X. Wu, G. Xu, Simulation of freefall water entry of a finite wedge with flow detachment, *Applied Ocean Research* 65 (2017) 262–278.
- [33] C. W. Hirt, B. D. Nichols, Volume of fluid (VOF) method for the dynamics of free boundaries, *Journal of Computational Physics* 39 (1) (1981) 201–225.
- [34] S. Muzaferija, M. Peric, P. Sames, T. Schellin, A two-fluid Navier-Stokes solver to simulate water entry, in: *Proceedings of 22nd symposium on naval architecture*, 1998, National Academy Press, 1998, pp. 277–289.
- [35] X. Zhang, P. Liu, Q. Qu, Y. Zhao, T. Hu, R. K. Agarwal, Numerical analysis of the pressure peak position shift with deadrise angle in two-dimensional wedge water entry, *Journal of Fluids Engineering* 140 (11) (2018) 111101.
- [36] X. Wen, P. Liu, Q. Qu, T. Hu, Impact of wedge bodies on wedge-shaped water surface with varying speed, *Journal of Fluids & Structures* 92 (2020) 102831. doi:10.1016/j.jfluidstructs.2019.102831.
- [37] D. Battistin, A. Iafrati, A numerical model for the jet flow generated by water impact, *Journal of Engineering Mathematics* 48 (3-4) (2004) 353–374.

- [38] Q. Qu, M. Hu, H. Guo, P. Liu, R. K. Agarwal, Numerical simulation of water-landing performance of a regional aircraft, *Journal of Aircraft* 52 (5) (2015) 1550–1558.
- [39] J. Wang, O. M. Faltinsen, Improved numerical solution of dobrovol'skaya's boundary integral equations on similarity flow for uniform symmetrical entry of wedges, *Applied Ocean Research* 66 (2017) 23–31.
- [40] S.-L. Chuang, Experiments on flat-bottom slamming, *Journal of Ship Research* 10 (01) (1966) 10–17.
- [41] S.-L. Chuang, Investigation of impact of rigid and elastic bodies with water, The Catholic University of America, 1969.
- [42] W. K. Meyerhoff, Added masses of thin rectangular plates calculated from potential theory, *Journal of Ship Research* 14 (02) (1970) 100–111.